

Structural characterization of (Sm,Tb)PO₄ solid solutions and pressure-induced phase transitions

Heuser, J. M.; Palomares, R. I.; Bauer, J. D.; Lozano Rodriguez, M. J.; Cooper, J.;
Lang, M.; Scheinost, A. C.; Schlenz, H.; Winkler, B.; Bosbach, D.; Neumeier, S.;
Deissmann, G.;

Originally published:

April 2018

Journal of the European Ceramic Society 38(2018), 4070-4081

DOI: <https://doi.org/10.1016/j.jeurceramsoc.2018.04.030>

Perma-Link to Publication Repository of HZDR:

<https://www.hzdr.de/publications/Publ-26663>

Release of the secondary publication
on the basis of the German Copyright Law § 38 Section 4.

CC BY-NC-ND

Structural characterization of (Sm,Tb)PO₄ solid solutions and pressure-induced phase transitions

J. M. Heuser^{a,b,*}, R. I. Palomares^c, J. D. Bauer^d, M. J. Lozano Rodriguez^e, J. Cooper^c, M. Lang^c, A. C. Scheinost^e, H. Schlenz^a, B. Winkler^d, D. Bosbach^a, S. Neumeier^a, G. Deissmann^a

^aForschungszentrum Jülich GmbH (FZJ), Institute of Energy and Climate Research (IEK-6), 52425 Jülich, Germany

^bPresent address: Karlsruhe Institute of Technology (KIT), Institute for Applied Materials (IAM), 76021 Karlsruhe, Germany

^cUniversity of Tennessee, Department of Nuclear Engineering, Knoxville, TN 37996, USA

^dGoethe University Frankfurt, Institute of Geosciences, Department of Crystallography, 60438 Frankfurt a. M., Germany

^eHelmholtz-Zentrum Dresden Rossendorf (HZDR), Institute of Resource Ecology, 01328 Dresden, Germany

*corresponding author: julia.heuser@kit.edu (J. M. Heuser)

Abstract

Sm_{1-x}Tb_xPO₄ solid solutions were synthesized and extensively characterized by powder X-ray diffraction, vibrational spectroscopy, and X-ray absorption spectroscopy. At ambient conditions solid solutions up to $x = 0.75$ crystallize in the monazite structure, whereas TbPO₄ is isostructural to xenotime. For $x = 0.8$ a mixture of both polymorphs was obtained. Moreover, a phase with anhydrite structure was observed coexisting with xenotime, which was formed due to mechanical stress. Selected solid solutions were investigated at pressures up to ~40 GPa using *in situ* high pressure synchrotron X-ray diffraction and *in situ* high pressure Raman spectroscopy. SmPO₄ and Sm_{0.5}Tb_{0.5}PO₄ monazites are (meta)stable up to the highest pressures studied here. TbPO₄ xenotime was found to transform into the monazite structure at a pressure of about 10 GPa. The transformation of Sm_{0.2}Tb_{0.8}PO₄ xenotime into the monazite polymorph commences already at about 3 GPa. This study describes the reversibility of the pressure-induced (Sm,Tb)PO₄ xenotime-monazite transformation.

Keywords

monazite, xenotime, anhydrite, solid solutions, phase transformation

Introduction

Natural monazite and synthetic orthophosphates with monazite structure, i.e. monoclinic $LnPO_4$ ($Ln = La-Gd$), have been subject to extensive research in the last decades. Natural monazites have extensively been used in geochronological studies for age determination of minerals and rocks (e.g. [1-5]) and serve as major source for rare earth elements and thorium (e.g. [6-8]). Due to their outstanding materials' properties, synthetic monazite-type materials have been proposed and used as thermal and diffusion barrier coatings (e.g. [9-14]), ionic conductors [15,16], heterogeneous catalysts [17], as well as electronic and optical devices [18-20]. Moreover, monazite-type ceramics are under consideration as potential nuclear waste forms for the safe disposal of plutonium and/or minor actinides (MA: Np, Am, Cm), due to their high structural flexibility for actinide incorporation, their resilience against radiation-induced amorphisation, and their chemical durability (cf. [21-29]).

At ambient conditions $LnPO_4$ crystallizes in either of two crystal structures, depending on the size of the Ln cations. Orthophosphates of the lighter and larger lanthanides ($Ln = La-Gd$) form the monazite structure-type (monoclinic with space group $P 2_1/n$ (C_{2h}^5)), while those of the heavier and smaller lanthanides ($Ln = Tb-Lu$) exhibit the xenotime structure, which is isostructural to the tetragonal zircon structure ($I 4_1/amd$ (D_{4h}^{19})) [7,30].

Lanthanide orthophosphates with $Ln = \text{Gd, Tb, Dy}$ show polymorphism at ambient conditions, i.e., one of two structure types can be quenched to exist metastably (e.g. [31,32]). The monazite and xenotime structure-types exhibit similar $Ln\text{O}_7\text{-PO}_4$ chains along the [001] direction. While the monazite structure is built up on irregular $Ln\text{O}_9$ polyhedra and slightly irregular (distorted) PO_4 tetrahedra, the xenotime structure has Ln cations regularly coordinated by eight oxygen atoms ($Ln\text{O}_8$) as well as regular PO_4 tetrahedra. Both, monazite and xenotime type phosphates have extensively been studied in the past, for example with respect to their crystal structure, miscibility, microstructure, thermodynamic properties, and dissolution behaviour (e.g. [7,30,33-39]).

The present work is related to research on the potential application of Sm-monazite as waste form for specific radioactive waste streams (e.g., separated Pu or Pu-contaminated materials). Sm ($Z = 62$) is one of those lanthanides whose orthophosphates crystallize in the monazite structure. The formation of solid solutions, for example due to the incorporation of actinides (as in potential monazite waste forms), requires that the substituting cation has a radius similar to that of the substituted cation. Due to the size of Sm^{3+} ($r = 1.132 \text{ \AA}$, CN = 9) [40] Sm-monazites can easily incorporate relevant radionuclides (e.g., Pu, Am, Cm) which exhibit both, slightly larger and slightly smaller cationic radii (cf. [40]). A profound understanding of the structural behaviour of these solid solutions as a function of chemical composition is essential for realistic assessments of their applicability as a waste form for radioactive waste management. The ionic radii of the substituting cations (e.g. in the case of tetravalent actinides) can be similar to those cations for which the endmembers would crystallize in the xenotime structure. Hence, it is essential to gain an in-depth understanding of the stability and flexibility of the monazite structure and the consequences of a structural change into the xenotime structure. Therefore, the structural response to Tb incorporation into Sm-monazite was investigated here. As TbPO_4 crystallizes in the xenotime structure, a study of $\text{Sm}_{1-x}\text{Tb}_x\text{PO}_4$ solid solutions will provide fundamental information on the role of the size match or mismatch between the substituting and substituted ion. In addition, pressure can be used to investigate the effect of relative changes in the ionic radii on the response to extreme conditions.

A structural classification of ABX_4 phases is given by the Bastide diagram (fig. 1) [41,42]. According to the classical Bastide diagram for ABX_4 compounds [41], phases crystallising in the xenotime structure at ambient pressure are predicted to have high-pressure modifications with the monazite structure type, as the r_A/r_B , r_B/r_X ratio is shifted to larger values with increasing pressure, due to the larger compressibility of the anion complexes. This is consistent with the observation that TbPO_4 -xenotime shows a transition to monazite at about 10 GPa [43-45]. The process of the phase transformation from xenotime to monazite was also intensively studied by Hay et al. [42,46,47,48,49]. However and in contrast to the present work, no high-pressure experiments were performed, but phase transitions were investigated in $(\text{Gd,Dy})\text{PO}_4$ xenotimes during nano indentation and fibre push-out tests. According to Hay et al. [42] the xenotime-monazite transition is a martensitic phase transformation [50] showing a shearing of different habitus planes. In contrast to this behaviour, Ln -monazites seem to remain stable on pressure increase and no phase transformations have been observed up to high pressures (CePO_4 up to 20 GPa [51], $(\text{Nd,Eu,Gd})\text{PO}_4$ up to 30 GPa [52], $(\text{Bi,Lu,Ce,Pr})\text{PO}_4$ up to 30, 25, 29, and 29 GPa, respectively [53], CaThPO_4 cheralite (isomorphous to monazite) up to 36 GPa [54]). One known exception is La-monazite that transforms into a post-barite type structure at about 26 GPa pressure [52,55].

To the best of our knowledge the response of $Ln\text{PO}_4$ solid solutions containing both monazite- and xenotime-type phases to high pressure has not been investigated so far. The present study therefore aims to contribute to the understanding of the structural response of the monazite crystal structure type on cation substitution by elucidating the phase stabilities, their long- and short-range order, and pressure-induced changes in

$\text{Sm}_{1-x}\text{Tb}_x\text{PO}_4$ solid solutions, thus contributing to a better understanding of monazite as a potential host phase for radionuclides in nuclear waste management [32].

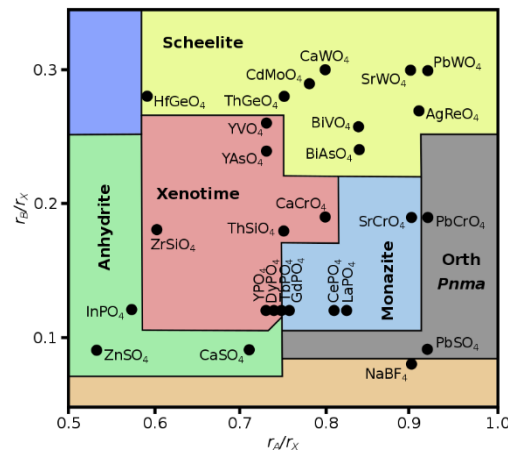


Fig. 1 Modified Bastide diagram after [42] showing the stability fields of various ABX_4 structures with respect to their ionic radii ratios. With increasing pressure both radii ratios (i.e., r_A/r_X , r_B/r_X) increase, leading to a southwest-northeast reaction path for pressure-induced phase transformations.

Materials and methods

Sample synthesis and structural characterization

Solid solutions in the system $\text{Sm}_{1-x}\text{Tb}_x\text{PO}_4$ ($x = 0$ to 1) were synthesized at ambient temperature *via* a co-precipitation route similar to that described by [56]. First, aqueous lanthanide (*Ln*) nitrate solutions were mixed in the desired molar ratios. Citric acid (CA) as a chelating agent was poured into this mixture in a molar ratio of $\text{Ln}:\text{CA} = 1:2$. Subsequently, an excess of phosphoric acid (P) was added ($\text{Ln}:\text{P} = 1:5$). To obtain a complete precipitation, the pH was adjusted to ~ 10 using 25 % NH_4OH while stirring. After drying at 90 °C, the precipitates were calcined (550 °C, 3 h) and sintered (1600 °C, 5 h). The samples were ground in an agate mortar after each thermal treatment step. In addition, pellets were fabricated from the calcined powders by uniaxial pressing (60 kN) and sintered as described before. The pellets were not polished to prevent contamination by the grinding material. The lanthanide ratio in the $\text{SmPO}_4\text{-TbPO}_4$ solid solutions was verified *via* energy dispersive X-ray spectroscopic (EDS) analyses on pellet samples, using a scanning electron microscope (SEM) (Quanta 200F, FEI) equipped with an Apollo X silicon drift Detector (EDAX). The phosphate phases were measured at five positions with a magnification of 6000x and a working distance of 10 mm in a low-pressure vacuum (60 Pa) using an acceleration potential of 20 kV.

X-ray diffraction (XRD) analyses were performed with a D4 ENDEAVOR diffractometer (Bruker AXS GmbH) using Cu radiation ($\lambda \text{ Cu K}\alpha_1 = 1.5405 \text{ \AA}$) at a power setting of 40 kV and 40 mA. Powder XRD patterns were collected at ambient conditions in the 2θ range from 10 to 130° using a step size of $0.02^\circ/2\theta$ and a counting time of 4 s per step. EVA software (Bruker AXS GmbH) was used for qualitative phase analysis. Structure refinements were performed employing the Rietveld method [57] as implemented in the Topas-Academic software (Version V4.1; [58]), using the fundamental parameter approach for X-ray line-profile fitting [59]. In the refinement, a six coefficient background polynomial, crystallite size, sample height/displacement, lattice parameters and fractional coordinates for all sites were allowed to vary. A potential preferential orientation of the xenotime phase (010) was considered with spherical harmonics. As starting models, the monazite and

xenotime structures from [30] were used. For the anhydrite structured (Sm,Tb)PO₄ phase, the structural model for CaSO₄ published by [60] was used.

X-ray absorption fine structure spectroscopy measurements were carried out on powdered samples which were diluted with boron nitride powder and pressed into pellets. Sm L₃ (6716 eV) edge and Tb L₃ (7514 eV) edge X-ray absorption fine-structure (XAFS) spectra were collected at ambient temperature at the Rossendorf Beamline (ESRF, Grenoble, France). A water-cooled, 1.4-m long, Rh-coated, meridionally-bent silicon mirror was used for beam collimation into a water-cooled Si(111) double crystal monochromator. The monochromatic beam was then focussed onto the sample by a 1.3-m long, Rh-coated, toroidal silicon mirror, achieving a rejection of higher order harmonics by at least four orders of magnitude. Several spectra were collected either in transmission mode using gas-filled ionization chambers, or in fluorescence mode using a 13-element high-purity Ge solid-state detector (Canberra) with digital signal treatment (XIA X-Map), energy-calibrated using the absorption edge of a Mn foil (6539 eV), and averaged to improve the signal-to-noise ratio using Sixpack [61].

Extended X-ray absorption fine-structure (EXAFS) spectra were extracted from the experimental XAFS spectra using WinXAS [62] following routine procedures. Spectra were normalized by fitting first-order polynomials to the pre-edge and second-order polynomials to the post-edge region, and then converted into *k*-space by arbitrarily assigning the first edge inflexion point to the onset of kinetic energy of the photoelectron. The EXAFS spectra were then extracted by fitting spline functions to the post-edge region using the auto-background module of WinXAS. The *k*³-weighted EXAFS spectra were then Fourier-transformed using a Bessel window with the Bessel parameter set to three. The local structure was determined by shell-fitting (WinXAS) using theoretical phase shift and amplitude functions calculated by FEFF8.2 [63] based on the structure of Sm monazite and Tb xenotime [30].

Raman spectra were recorded at ambient pressure using a Jobin-Yvon Aramis LabRam HR Micro-Raman spectrometer (Horiba Scientific) on sintered (Sm,Tb)PO₄ pellets, employing the 632.8 nm line of a He-Ne laser as the excitation wavelength. Spectra were recorded in the wavenumber range of 100 to 1200 cm⁻¹. For each spectrum, an acquisition time of 10 to 25 s was used with an average of 2 scans. Peak positions were analysed using the HORIBA LabSpec software (version 5.58.25) after fitting the Raman modes using Gaussian-Lorentzian mixed functions.

Infrared (IR) spectra were obtained with a FT-IR Bruker Equinox 55 instrument using the KBr pellet method. Spectra were recorded in the wavenumber interval from 400 cm⁻¹ to 4000 cm⁻¹ with a resolution of 2 cm⁻¹. For the measurements, 1 mg of sample was mixed with 250 mg KBr, pelletized and measured immediately after preparation under ambient conditions in air. Data analysis was performed using the Opus software (version 4.0, Bruker).

High-pressure experiments

High-pressure synchrotron X-ray diffraction experiments were performed in order to investigate high pressure structural transformations on the endmembers and selected intermediate compositions at pressures up to ~40 GPa. Each sample was loaded into a 120-150 μm hole that was drilled into a Re gasket pre-indented to 25-35 μm. The gaskets were used with symmetric diamond-anvil cells (DACs) with either 400 μm (SmPO₄ and TbPO₄) or 300 μm (Sm_{0.5}Tb_{0.5}PO₄ and Sm_{0.2}Tb_{0.8}PO₄) diamond culets. Neon gas was used as the pressure-transmitting medium and the pressure was determined using the ruby fluorescence technique. The experiments were carried out at the 16-BM-D station of the High Pressure Collaborative Access Team (HPCAT) sector at the Advanced Photon Source (APS) using a 5 x 5 μm² (FWHM) focused beam of 29.2 keV X-rays (λ = 0.4246 Å). Angle-dispersive XRD measurements were collected as a function of pressure in transmission mode

using a MAR345 image plate detector. The detector was calibrated using a NIST CeO₂ standard and the XRD images were integrated into one-dimensional patterns using the Dioptas software [64]. Derivation of the instrument parameters was performed with the XRD pattern of the CeO₂ standard and Rietveld refinement of the XRD patterns was conducted in the GSAS-II software [65].

For high-pressure Raman experiments, powder samples were loaded in Boehler-Almax type [66] DAC. Tungsten foil of an initial thickness of ~200 µm was used as a gasket material. The gasket was pre-indented to a thickness of about 80 µm and a hole with a diameter of about 150 µm was laser-drilled into the gasket to serve as sample chamber. A small ruby chip (easyLab Technologies Ltd, Reading, UK) was loaded into the sample chamber for pressure determination with the ruby fluorescence method [67]. Neon was used as pressure transmitting medium. The gas was loaded with a custom-built gas loader at 0.18 GPa. The maximum pressure reached in the Raman study was about 20 GPa.

Confocal micro-Raman measurements at high-pressure were carried out with a Renishaw Raman spectrometer (RM-100) equipped with a Leica DMLM optical microscope with a grating with 1800 grooves/mm and a Peltier-cooled charge-coupled device (CCD). For excitation the 632.81 nm line of a He-Ne laser with a maximum power of 50 mW was used. A 20x objective lens with long working distance and a quasi-backscattering geometry was employed. The spectra were collected in the range of 100 cm⁻¹ to 1200 cm⁻¹ with exposure times of 60 s and a laser power of up to 100 % of the maximum power. The system was calibrated using the band at 519 cm⁻¹ of a Si wafer [68]. The accuracy of the wave numbers was ~1 cm⁻¹ and the spectral resolution 2 cm⁻¹. Due to the use of a notch filter our experimental set-up only allows to measure Raman shifts >100 cm⁻¹. Data were processed using the HORIBA Scientific software LabSpec (5.58.25) using Gaussian Lorentzian mixed functions to fit the Raman bands.

Results and discussion

Phase analyses and structural long range order

X-ray diffraction analysis was performed for phase analysis on the one hand and to investigate the structural long range order within the solid solution on the other hand. XRD patterns of the as prepared Sm_{1-x}Tb_xPO₄ solid solutions including the endmembers are shown in figure 2. The data show that in samples up to $x = 0.75$ monazite is the main phase. However, a polymorph with the xenotime structure appears in traces in samples with compositions of $x \geq 0.65$ (cf. table 1). For $x = 0.8$ polymorphs with monazite and xenotime structure can be found in about equal amounts, while xenotime is the main phase for $x = 1$. Furthermore, in powder samples with $x \geq 0.8$ small amounts (<10 wt%) of another (Sm,Tb)-orthophosphate having the anhydrite structure were detected [32]; however, this phase was not observed in sintered pellets. Lanthanide phosphates with anhydrite structure only occur in powder samples coexisting with xenotime as the predominant phase. The occurrence of the different phases depending on the nominal sample composition is summarized in table 1.

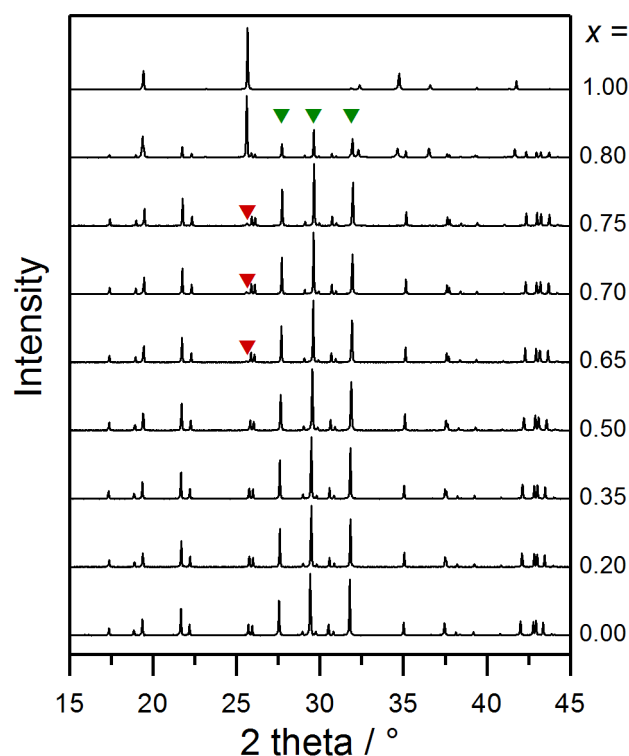


Fig. 2 Characteristic powder diffraction patterns of selected $\text{Sm}_{1-x}\text{Tb}_x\text{PO}_4$ solid solutions as well as the Sm- and Tb-endmember ($x = 0$ and 1 , respectively). Characteristic reflections to distinguish monazite (green) and xenotime (red) are marked in selected powder patterns.

Table 1 Phase occurrence in sintered (1600°C) $\text{Sm}_{1-x}\text{Tb}_x\text{PO}_4$ solid solutions (powder samples): Main phase (\blacklozenge), minor phase (\blacklozenge) or traces $< 1.5 \text{ wt}\%$ (\blacklozenge).

x	0.0	0.2	0.35	0.5	0.65	0.7	0.75	0.8	1.0
Monazite	\blacklozenge	\blacklozenge	\blacklozenge	\blacklozenge	\blacklozenge	\blacklozenge	\blacklozenge	\blacklozenge	-
Xenotime	-	-	-	-	\blacklozenge	\blacklozenge	\blacklozenge	\blacklozenge	\blacklozenge
Anhydrite	-	-	-	-	-	-	-	\blacklozenge	\blacklozenge

The three $(\text{Sm,Tb})\text{PO}_4$ -phases coexisting in the sintered $\text{Sm}_{0.2}\text{Tb}_{0.8}\text{PO}_4$ powder can be distinguished also in SEM micrographs due to their distinct morphologies (fig. 3a), whereas in the corresponding pellets only two coexisting phosphate phases, namely monazite and xenotime, occur (fig. 3b). The EDS analyses revealed that, within the error of the applied analytical method, both the monazite and xenotime phase have an identical chemical composition of stoichiometric $\text{Sm}_{0.2}\text{Tb}_{0.8}\text{PO}_4$.

Due to the coincidence of the main diffraction maxima of xenotime and the (Sm,Tb) -phosphate with anhydrite structure, the structural refinement for the latter phase was limited to the lattice parameters. The detailed results of the Rietveld refinements are compiled in tables S1 and S2 in the supporting information. The data for the endmembers, i.e., SmPO_4 (monazite) and TbPO_4 (xenotime) are in good agreement with published structural data (cf. [28,30]).

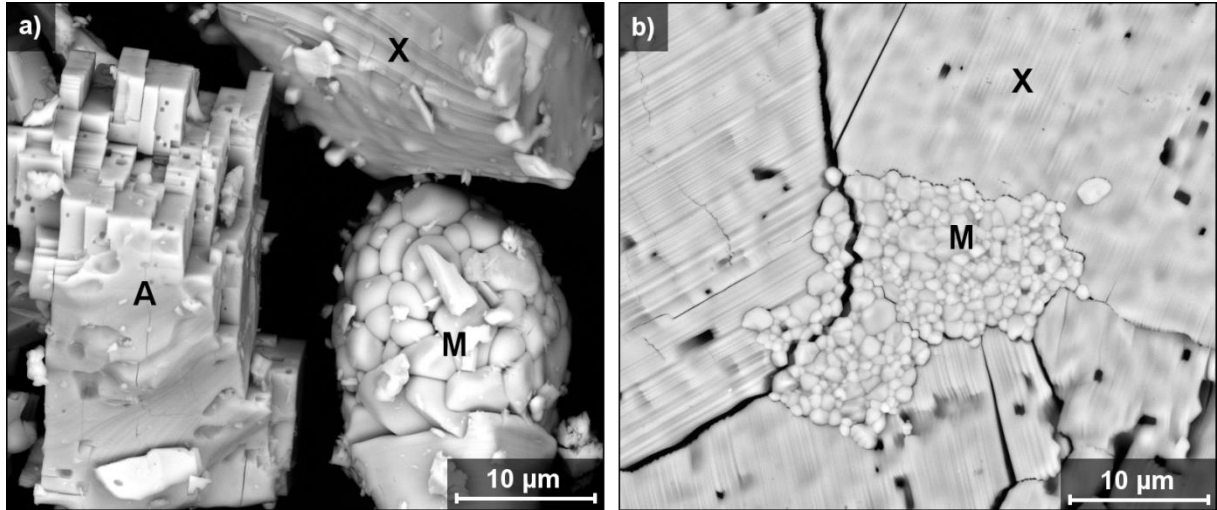


Fig. 3 a) SEM micrograph (BSE detector) of a sintered $\text{Sm}_{0.2}\text{Tb}_{0.8}\text{PO}_4$ powder; X = xenomorphic xenotime grain showing twinning, M = roundish monazite grains, A = phosphate in anhydrite structure showing a blocky habitus. b) SEM micrograph (BSE detector) of a sintered $\text{Sm}_{0.2}\text{Tb}_{0.8}\text{PO}_4$ pellet; Xenotime (X) occurs as large grains (20-60 nm) exhibiting polysynthetic twinning, while monazite (M) is aggregated in fine-grained (2-5 nm) regions.

The lattice parameters of the $(\text{Sm,Tb})\text{PO}_4$ -monazites depend linearly on composition and decrease with increasing Tb-content, while the monoclinic angle β increases (fig. 4). This behaviour is qualitatively expected due to the smaller ionic radius of Tb^{3+} (1.095 Å; CN = 9) compared to Sm^{3+} (1.132 Å; CN = 9) (cf. [40]). The linear trends in the lattice parameters following Vegard's law confirm the formation of monazite-type solid solutions in the $\text{Sm}_{1-x}\text{Tb}_x\text{PO}_4$ -system up to $x = 0.8$. The average Ln-O bond length in the monazite-type solid solutions decreases with increasing Tb-content, from 2.493 Å (SmPO_4) to 2.467 Å ($\text{Sm}_{0.25}\text{Tb}_{0.75}\text{PO}_4$); the Ln-O bond length value obtained for the $\text{Sm}_{0.2}\text{Tb}_{0.8}\text{PO}_4$ -monazite (2.492 Å) is questionable, due to difficulties with the Rietveld refinement caused by the presence of the anhydrite-type phase using the available laboratory XRD powder patterns [32]. Generally, the Ln-O bond length is shorter than the sum of the average ionic radii (2.512 Å for Sm-O and 2.475 Å for Tb-O, CN = 9) indicating some covalent bonding. As expected, the average Ln-O bond length for the eightfold coordinated Ln-ions in the xenotime solid solutions are significantly shorter (cf. [30]), with the shortest bond length in the TbPO_4 endmember (2.35 Å). The P-O bond lengths in the monazite solid solutions is rather constant (1.56 ± 0.01 Å), which is in good agreement with the P-O distance of an ideal PO_4 tetrahedron (1.55 Å).

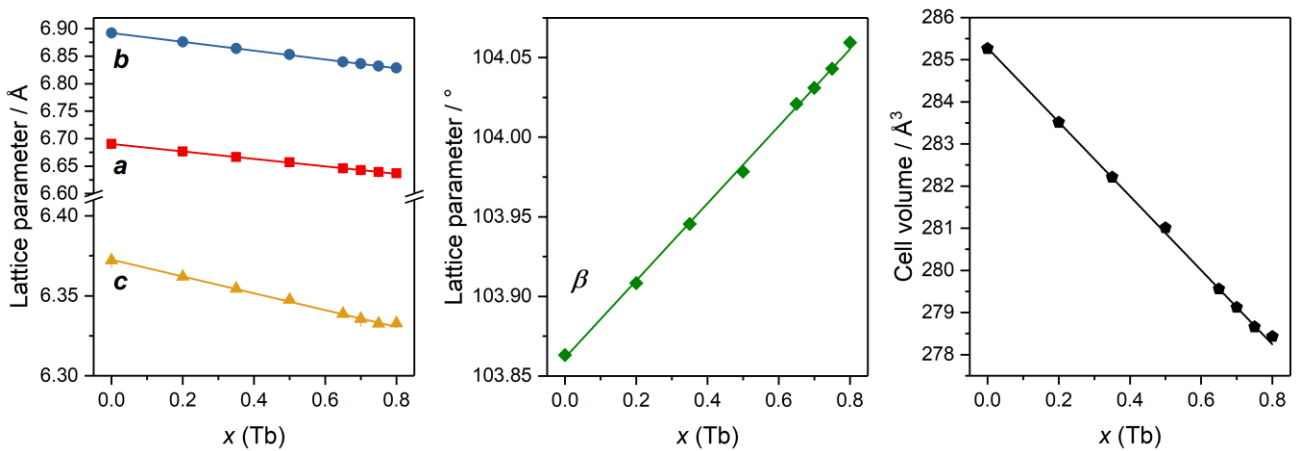


Fig. 4: Powder XRD results for $\text{Sm}_{1-x}\text{Tb}_x\text{PO}_4$ monazite phases as a function of x (Tb): Lattice parameters a , b , c (left) and β (middle) as well as the unit cell volume (right). The error bars are in the size of the symbol.

Structural short range order

Complementary to the XRD investigations, vibrational spectroscopy (i.e., IR and Raman) was applied to address the short range order in the system $(\text{Sm,Tb})\text{PO}_4$. Figure 5 (left) depicts the IR spectra of the $\text{Sm}_{1-x}\text{Tb}_x\text{PO}_4$ samples, focussing on the wavenumber range that is influenced by PO_4 modes of monazite and xenotime. In the IR spectra, the two polymorphs monazite and xenotime are evidenced, whereas no anhydrite type Ln -phosphate was observed at $x \geq 0.8$. Representative spectra for a monazite-type structure were obtained for the monazite solid solutions with $x \leq 0.75$, showing all IR active vibrations related to the stretching and bending of the PO_4 group of monazite (cf. [69,70]). A broad band between 1104 and 1003 cm^{-1} and a narrower, sharper band at 962 to 966 cm^{-1} can be assigned to antisymmetric (ν_3) and symmetric (ν_1) stretching modes, respectively. The antisymmetric bending modes (ν_4) are located between 631 and 540 cm^{-1} , while the precise position of the symmetric bending mode (ν_2) ($\sim 490\text{ cm}^{-1}$), occurring at the shoulder of ν_4 , is difficult to ascertain. The TbPO_4 endmember shows a spectrum typical for xenotime-type structures, lacking the modes related to symmetric vibrations, due to its higher symmetry (cf. [69,71]). For the sample with the nominal composition $x = 0.8$, containing approximately equal amounts of monazite and xenotime, a mixed spectrum was obtained with undetectable ν_1 and ν_2 modes.

Within the Sm-Tb-monazite solid solution series, the position of the IR modes shifts to higher wavenumbers with increasing Tb-contents (cf. figure S1 in the supporting material) due to the decrease in the length of the Ln-O bonds and the resulting lattice contraction. The split-up of the ν_4 mode and partly its intensity decreases with an increasing content of the smaller Tb-ions, indicating a concomitant decrease in the distortion of the PO_4 -tetrahedra in the monazite structure [32,72].

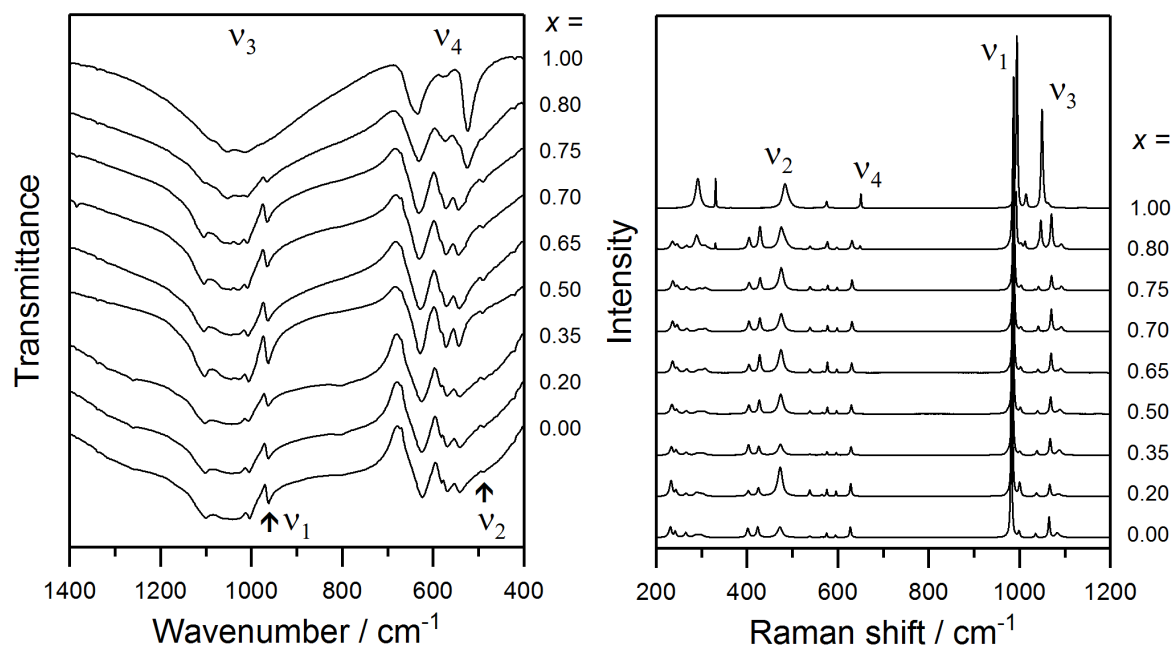


Fig. 5 Vibrational spectra of $\text{Sm}_{1-x}\text{Tb}_x\text{PO}_4$: IR spectra (left) and Raman spectra (right).

The Raman spectra are depicted in figure 5 (right). Spectra characteristic for monazite- and xenotime-type structures were observed for $x \leq 0.75$ and $x = 1$, respectively. Both phases were observed for $x = 0.8$ resulting in a mixed spectrum. According to factor group analysis, 36 Raman active modes are allowed for monazite-type structures, however not all could be identified unambiguously. Especially the modes related to the

bending and stretching of the phosphate group are clearly evident in the spectra. For the monazite-type solid solutions, the ν_1 , ν_2 , ν_3 and ν_4 vibrations were observed in the range from 981 to 988 cm^{-1} (symmetrical stretching mode), 473 to 475 cm^{-1} (symmetrical bending mode), 1065 to 1070 cm^{-1} (antisymmetrical stretching mode) and 628 to 631 cm^{-1} (antisymmetrical bending mode), respectively. In the pure TbPO_4 xenotime not all 17 expected Raman modes were observed, however all nine expected belonging to the normal modes of the PO_4 tetrahedra.

In figure 6, the Raman shifts of the ν_1 to ν_4 modes of the $\text{Sm}_{1-x}\text{Tb}_x\text{PO}_4$ samples are plotted vs. the mole fraction of Tb. In addition to the previously mentioned xenotime phase at $x = 1$, also data for TbPO_4 in monazite structure from another synthesis [32] is given (cf. fig. 6 open symbols). For $x \leq 0.8$ the four modes ν_1 to ν_4 show a linear increase of the wavenumbers with increasing Tb content, confirming the formation of monazite-type (Sb,Tb) PO_4 solid solutions. Although this blue shift was already reported previously for monazite solid solutions (e.g. [39,73-75]), its origin is still debated. Begun et al. [76] and Hobart et al. [77] proposed the compression of the PO_4 -tetrahedron, resulting in shorter P-O distances and a denser packing of the polyhedra as a cause for the higher vibration frequencies. Contrarily, Podor et al. [78] and Santos et al. [79] attributed the blue shift to the lattice contraction resulting from decreasing Ln-O distances, while the phosphate tetrahedron is not compressed or further distorted. The structural data obtained by XRD indicate that the P-O distances in the (Sb,Tb)-monazites remain constant, while the average Ln-O bond length decreases with increasing Tb-content. Therefore, it is likely that the blue shift observed here can be attributed to the progressive lattice contraction originating from the increasing content of a smaller Ln-cation (here Tb) in the monazite structure, as suggested also by Hirsch et al. [39] and Neumeier et al. [75] for $\text{La}_{1-x}\text{Ln}_x\text{PO}_4$ -monazites (Ln = Pr, Gd, Eu).

With the change from the monazite structure to the xenotime structure at $x \geq 0.8$, a significant jump in the wavenumbers of the main modes of the ν_1 , ν_2 and ν_4 vibrations is observed. In contrast, the wavenumber of the B_{1g} mode of the antisymmetric stretching vibration ν_3 of xenotime is significantly lower compared to monazite. However, compared to the B_g -mode of the ν_3 -vibration of monazite (cf. fig. 6, grey symbols), the wavenumber of the ν_3 -vibration of xenotime is again higher (cf. [76]). These higher frequencies of the bending and stretching vibrations in the PO_4 -groups can be attributed to the closer restrictions imposed on the (undistorted) PO_4 -tetrahedra in the tetragonal xenotime structure and the stronger bonding forces in the eightfold coordinated LnO_8 polyhedra, compared to the LnO_9 polyhedra in monazite [32]. This effect seems to affect in particular the frequencies of the symmetrical and antisymmetrical bending vibrations ν_2 and ν_4 .

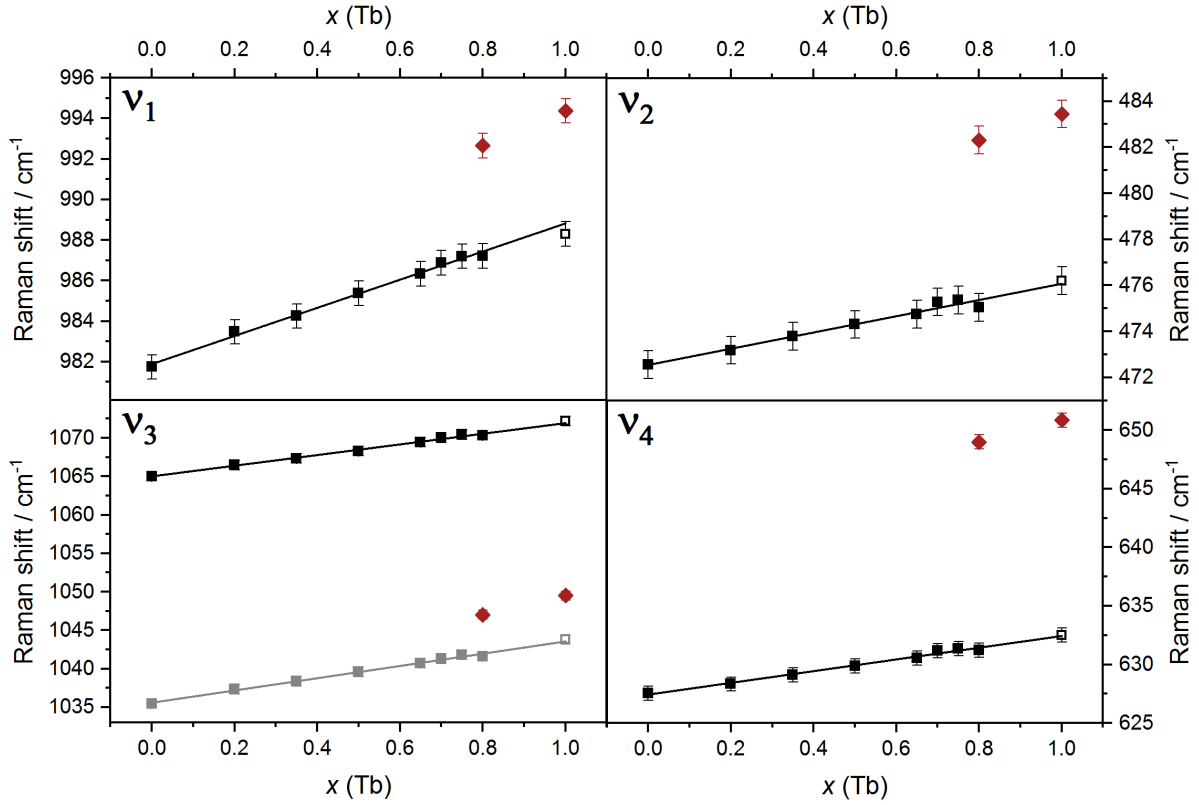


Fig. 6 Raman-peak shift behaviour of the normal modes ν_1 to ν_4 as a function of the Tb-content (x) in $\text{Sm}_{1-x}\text{Tb}_x\text{PO}_4$ for different phases: monazite (black/grey squares), xenotime (red diamonds) and Tb-monazite for comparison (open symbols; [32]; see text for more detailed information).

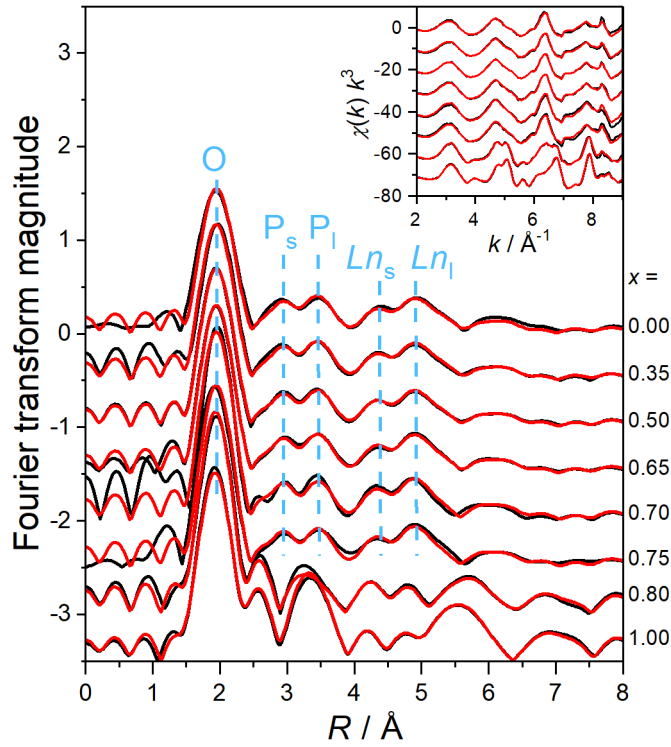


Fig. 7 Sm-L₃ EXAFS spectra of the $\text{Sm}_{1-x}\text{Tb}_x\text{PO}_4$ solid solutions up to $x = 0.8$, compared to the Tb-L₃ edge spectrum for $x = 1.00$. Black lines are the experimental spectra, red lines their reconstruction with two principal components. The large figure gives the k^3 -weighted Fourier transform magnitudes, the insert the k^3 -weighted chi-spectra. The position of the major backscattering contributions from O, P and lanthanide shells are given by blue dashed lines.

EXAFS was carried out to evaluate the local structure of the $\text{Sm}_{1-x}\text{Tb}_x\text{PO}_4$ solid-solutions between the Sm endmember with monazite and the Tb endmember with xenotime structure. Figure 7 shows from top to bottom the EXAFS spectra of the pure Sm-monazite endmember, of the Tb-doped Sm-phosphate samples sorted along increasing Tb atom-percent, and finally of the pure Tb-xenotime endmember.

Up to $x = 0.75$, the spectra of the $\text{Sm}_{1-x}\text{Tb}_x\text{PO}_4$ series are almost identical to the pure Sm monazite endmember. For $x = 0.8$, however, the spectrum has already many features of the xenotime endmember shown on the bottom. A principal component analysis using the ITFA analysis software package was performed to identify the number of statistically significant components in all spectra [80,81]. Both the Malinowski indicator calculated by ITFA as well as the good reproduction of the experimental spectra by two components as shown in figure 7 suggest that the local structure of the solid solutions consists of only two main structural motifs, a Sm-monazite and a Tb-xenotime motif. Assuming that the samples at $x = 0$ and $x = 1$ represent the pure monazite and xenotime endmember structures, their fractions in the solid solution series were determined by the iterative target test transformation module of ITFA (see table 2). In agreement with the visual observation, the spectra up to $x = 0.75$ are almost pure monazite-type, while the sample at $x = 0.8$ consists of the monazite and xenotime endmembers in equal amounts in accordance with the XRD data. Note that the ancillary (<10 %) anhydrite phase detected by XRD does not show up in the EXAFS as a separate phase, most likely because of its similar short-range structure.

Table 2. Mol fraction x of $\text{Sm}_{1-x}\text{Tb}_x\text{PO}_4$ monazite and xenotime determined by ITFA; data (wt%) from Rietveld refinement of XRD patterns shown in brackets for comparison.

x	Monazite	Xenotime
0.0	1.00 (100)	0.00 (0)
0.35	0.99 (100)	0.01 (0)
0.5	0.96 (100)	0.04 (0)
0.65	0.96 (99.4±0.1)	0.04 (0.6±0.1)
0.7	0.92 (98.8±0.1)	0.08 (1.2±0.1)
0.75	0.93 (98.7±0.1)	0.07 (1.3±0.1)
0.8	0.44 (45.7±0.3)	0.56 (50.3±0.3)
1.0	0.00 (0)	1.00 (91.1±0.3)

Table 3. EXAFS shell fit results of the Sm-monazite and the Tb-xenotime endmembers.

Sample	Path	CN	$R / \text{\AA}$	$\sigma^2 / \text{\AA}^2$	$\Delta E_0 / \text{eV}$	S_0^2	$\chi_{\text{res}} / \%$
SmPO ₄	Sm-O	9	2.44	0.0103	10.9	0.90	11.2
	Sm-P	2	3.24	0.0142			
	Sm-P	5	3.68	0.0120			
	Sm-Sm	3	3.98	0.0044			
	Sm-Sm	3	4.19	0.0030			
TbPO ₄	Tb-O	8	2.37	0.0050	14.3	0.90	8.6
	Tb-P	2	3.06	0.0027			
	Tb-P	4	3.79	0.0080			
	Tb-Tb	4	3.79	0.0056			
	MS	8	3.85	0.0050			

CN: coordination number, R : radial distance, σ^2 : Debye-Waller term, ΔE_0 : phase shift, S_0^2 : amplitude reduction factor, χ_{res} : residual error, MS: multiple scattering path.

Table 3 gives the fit results for the local structures of these two endmembers. With space group $P 12_1/n1$ (14), the monazite structure shows poor radial distribution ordering of the atoms around the cation centres.

In SmPO_4 the coordination shell of nine oxygen atoms has Sm-O distances ($R_{\text{Sm-O}}$) between 2.39 and 2.77 Å, two P atoms from phosphate units sharing edges with the SmO_9 polyhedra have distances between 3.13 and 3.25 Å, five P atoms from corner-sharing phosphate units have distances varying between 3.45 and 3.73 Å, followed by three Sm neighbours from 4.02 to 4.06 Å and another three Sm neighbours from 4.23 to 4.25 Å. Since the distal resolution of EXAFS is limited by $\pi/(2 \cdot \Delta\chi)$, shells have to be separated by at least 0.21 Å given the limited k -range available (2.0 to 9.5 Å⁻¹). Therefore, the different individual interatomic distances were grouped into shells for EXAFS fitting according to the scheme outlined above. The fitted distances shown in table 3 are in good agreement with published Sm monazite structure data [30].

Radial distances in the tetragonal xenotime structure are much more uniform, hence only for the Tb-O coordination shell two different distances had to be combined into one shell, while all further backscattering shells could be fitted based on the crystallographic data. The shorter Tb-P distances of 3.06 Å correspond to the edge-sharing phosphate groups and the longer Tb-P distances at 3.79 Å to the corner-sharing phosphate groups. The Tb-Tb distances at this latter distance result from edge-sharing TbO_8 -polyhedra. These fitted radial distances of the short-range structure are in good agreement with the long-range monazite structure (table 3) [30].

Discussion of the structural analyses:

Powder XRD, Raman as well as IR spectroscopy show a gradual incorporation of Tb into the Sm-monazite crystal structure up to $x = 0.8$. However, at $x = 0.8$ a xenotime phase coexists with the monazite phase in about equal amount. For higher Tb content, the xenotime phase replaces the monazite phase with regard to the chosen compositional steps. In contrast to XRD and the vibrational spectroscopy methods, EXAFS is able to reveal differences in the Ln-O bond lengths in the different compositions. An increasing tension going along with the Sm substitution by Tb occurs due to shorter Tb-O bond lengths and finally leads to the preferential formation of the xenotime structure.

Moreover, in compositions with $x \geq 0.8$ a minor phase with anhydrite structure is observed, coexisting with the xenotime phase. Ln-orthophosphates with anhydrite structure were first described by Hay et al. [46], who observed $\text{Gd}_{0.5}\text{Dy}_{0.5}\text{PO}_4$ and $\text{Gd}_{0.4}\text{Dy}_{0.6}\text{PO}_4$ in anhydrite structure as a result of a phase transformation from a xenotime-type phase during ball milling. Furthermore, a transformation from a xenotime-type phase into a polymorph with anhydrite-type structure was observed in TbPO_4 , $\text{Gd}_{0.3}\text{Tb}_{0.7}\text{PO}_4$, and $\text{Gd}_{0.4}\text{Dy}_{0.6}\text{PO}_4$ as effect of grinding or polishing pellet samples [42]. Tschauner et al. [82] published the first refined crystal structure for a rare-earth orthophosphate in anhydrite structure using single crystal XRD data suggesting the space group $C mcm$.

Hay et al. [42,46,47] explained the reversible transformation of xenotime-type Ln-orthophosphates into an anhydrite-type phase as a consequence of high shear stress, occurring at relatively low pressures (≤ 200 MPa). In general, the xenotime to anhydrite transformation is favoured with decreasing r_B/r_O and thus at low pressures [42]. Hay et al. [42] as well as Tschauner et al. [82] observed the transformation path xenotime \rightarrow anhydrite \rightarrow monazite with increasing pressure. However, Tschauner et al. [82] pointed out a deviation from the typical trend of equal polyhedral compression as described in the Bastide diagram. As this is not completely consistent with the typical trend of equal polyhedral compression [82] as described in the Bastide diagram, Hay et al. [42] expanded the stability field of the anhydrite structure of LnPO_4 in a modified Bastide diagram (see fig. 1). Moreover, the LnPO_4 polymorphs with the anhydrite structure were found to be stable up to sintering temperatures of 1400 °C [46], but did not occur at sintering temperatures as high as used within the present work (1600 °C). The occurrence of the $\text{Sm}_{1-x}\text{Tb}_x\text{PO}_4$ in anhydrite structure at $x \geq 0.8$ in powdered samples, and its absence in the unpolished pellet samples sintered at 1600 °C in the current study, is thus

thought to be the consequence of a partial transformation of the xenotime-type phase due to the shear stress inflicted during sample grinding.

High-pressure experiments

High-pressure-synchrotron XRD

High-pressure XRD experiments were performed in order to investigate the structural response of the endmembers SmPO_4 (monazite-type) and TbPO_4 (xenotime-type), as well as selected solid solution compositions, namely $\text{Sm}_{0.5}\text{Tb}_{0.5}\text{PO}_4$ (monazite) and $\text{Sm}_{0.2}\text{Tb}_{0.8}\text{PO}_4$ (monazite- + xenotime-type). XRD measurements were collected as a function of increasing and decreasing pressure and the data are presented in figure 8. Figure 9 shows the unit cell parameters a , b , and c as function of increasing pressure for all sample compositions studied.

In general, the two phases monazite and xenotime respond differently to elevated pressures. While monazite remains stable at high pressures, the xenotime phase undergoes a phase transformation into the monazite structure. In the following the high-pressure behaviour analysed by *in-situ* XRD measurements is described in detail for all four investigated compositions.

High-pressure XRD measurements on SmPO_4 monazite were performed up to a maximum pressure of 41 GPa (fig. 8a). Significant peak broadening was observed as the pressure was increased; however, no phase transformation from the starting monazite-type phase was evident. The broadening of diffraction maxima at higher pressures is likely due to an increase in heterogeneous microstrain caused by the quasi-hydrostatic pressure environment. During pressure release, the width of the diffraction maxima is decreasing again. The unit cell parameters a , b and c showed a linear decrease with increasing pressure due to the compression of the monazite structure (fig. 9a). Similarly, significant peak broadening without a structural transformation was observed with increasing pressure for $\text{Sm}_{0.5}\text{Tb}_{0.5}\text{PO}_4$ up to 33 GPa (fig. 8b). Also here, the unit cell parameters decrease steadily with an increase of pressure, however showing slight deviations from linearity (fig. 9b).

The $\text{Sm}_{0.2}\text{Tb}_{0.8}\text{PO}_4$ sample consists of a mixture of monazite- and xenotime-type polymorphs at ambient conditions (fig. 8c). At pressures of 9.6 GPa the intensities of the xenotime reflections decrease compared to that of the monazite-type phase. At pressures of and above 13.6 GPa, only the monazite-type phase is present and no other transformation was observed up to the maximum pressure applied in this experimental run (~20 GPa). Both phases reveal a linear decrease of their lattice parameters with increasing pressure (fig. 9c). The XRD pattern of the quenched sample shows again both phases, however the amount of monazite had increased compared to the initial sample. The TbPO_4 -endmember, which exhibits the xenotime structure at ambient conditions, underwent an analogous phase transformation into the monazite structure starting at 9.8 GPa with full completion at <16.8 GPa; no further phase transition occurred up to a pressure of ~21 GPa (fig. 8d, 9d). Up to a pressure of about 11.5 GPa, the xenotime structure is compressed linearly (cf. fig. 9d). With the transformation into the monazite structure, a distinct change in the c unit cell parameter occurs, corresponding to the larger c -axis in monazites compared to (isochemical) xenotimes. For example, at ambient pressure the c unit cell parameter of the (metastable) TbPO_4 -monazite is significantly larger (6.317 Å) compared to the corresponding unit cell parameter of TbPO_4 -xenotime (6.073 Å) (cf. [32]). Once the transformation to monazite is completed for TbPO_4 , the unit-cell parameters decrease linearly under further compression.

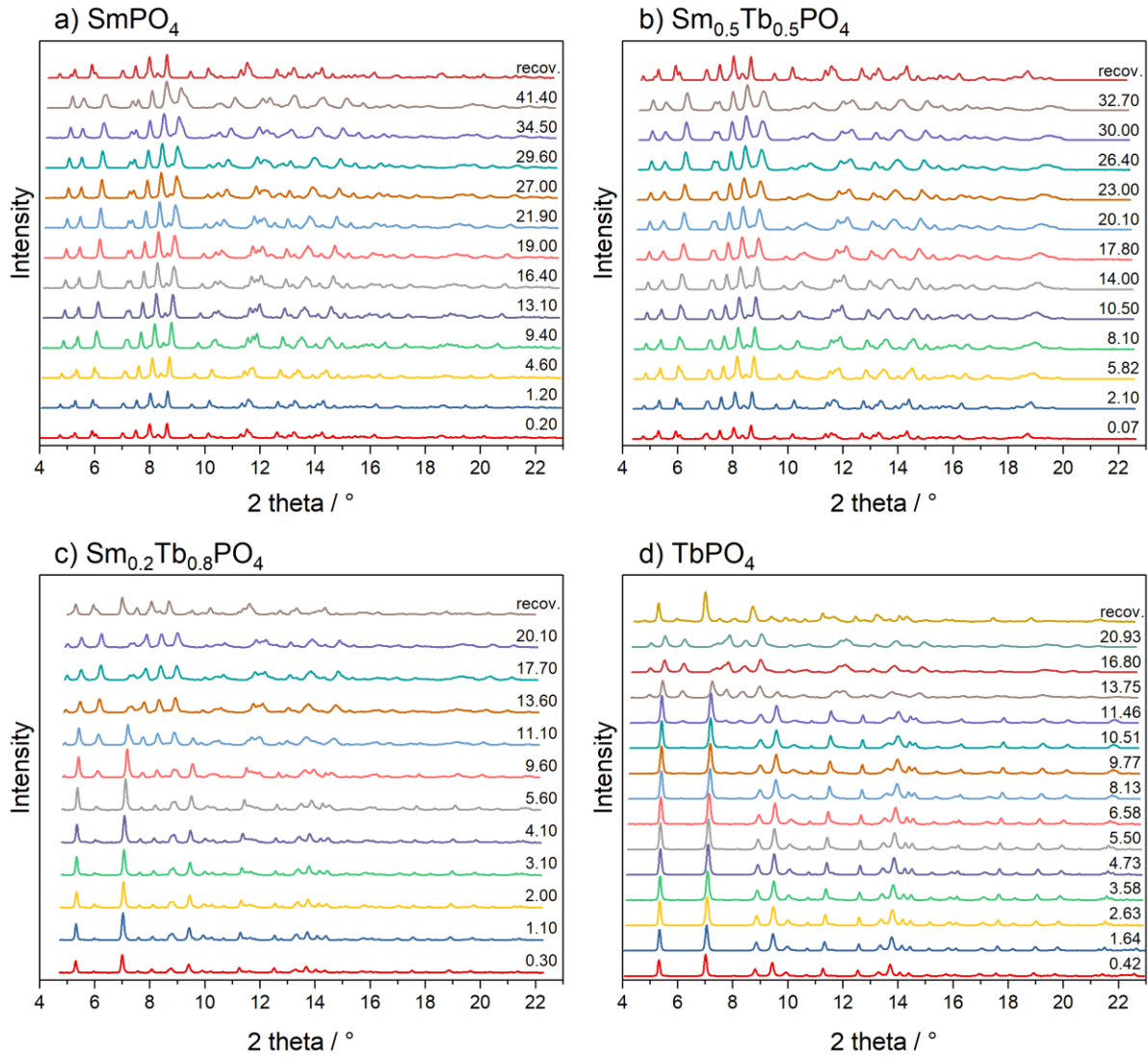


Fig. 8 High pressure synchrotron XRD patterns of $\text{Sm}_{1-x}\text{Tb}_x\text{PO}_4$ solid solutions collected as a function of increasing and decreasing pressure (recovered samples at ambient conditions on top). Pressure values are given in GPa.

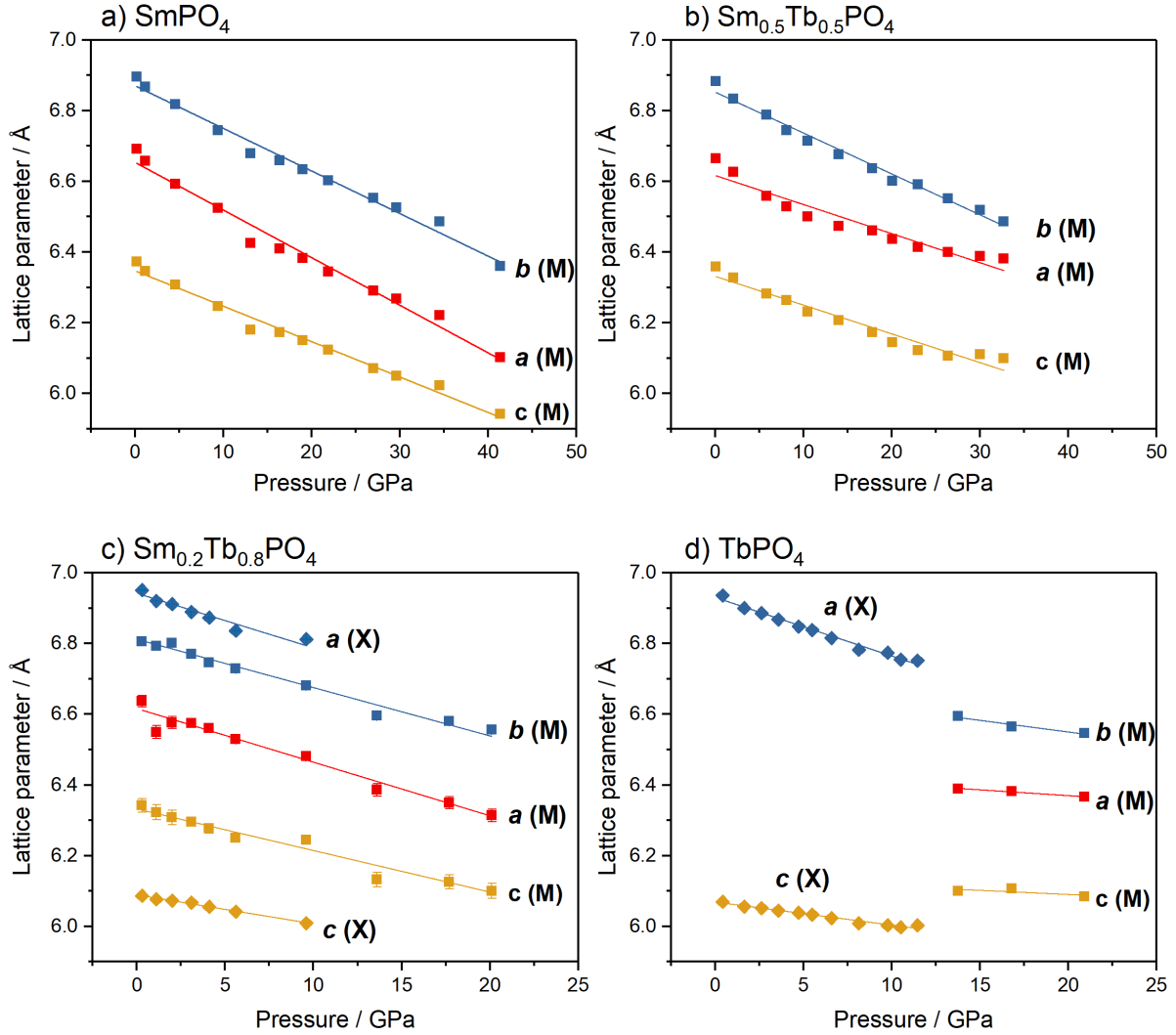


Fig. 9 Lattice parameters a , b , and c of $\text{Sm}_{1-x}\text{Tb}_x\text{PO}_4$ monazite (M) and xenotime (X) solid solutions as function of pressure. Please note: for d) TbPO_4 at pressures of about 10.5 and 11.5 GPa the monazite phase is present beside the predominant phase of xenotime, however the amount of monazite is too small to receive reliable lattice parameters. Moreover, xenotime is still present at 13.75 GPa, however no reliable lattice parameters could be obtained.

High-pressure Raman spectroscopy

To gain insights into pressure effects on the short-range order in $(\text{Sm},\text{Tb})\text{PO}_4$ solid solutions, high-pressure Raman experiments were performed using three specific compositions in the $\text{Sm}_{1-x}\text{Tb}_x\text{PO}_4$ series: $\text{Sm}_{0.5}\text{Tb}_{0.5}\text{PO}_4$ (monazite type), $\text{Sm}_{0.2}\text{Tb}_{0.8}\text{PO}_4$ (monazite- + xenotime-type), and pure TbPO_4 (xenotime-type). Again a different pressure dependent behaviour of monazite and xenotime was observed. Figure 10a shows selected Raman spectra of $\text{Sm}_{0.5}\text{Tb}_{0.5}\text{PO}_4$, which exhibits the monazite structure at ambient conditions, up to a pressure of 20.5 GPa.

As a function of increasing pressure all observed Raman modes shift to higher wavenumbers due to the compression of the crystal structure (cf. [51]). However, no pressure-induced phase transformation was observed and the spectrum of the recovered sample after pressure release (top in fig. 10a) is similar to the one before pressurisation. The pressure-induced shifts of the Raman modes depend linearly on the pressure and are fully reversible (fig. 11a).

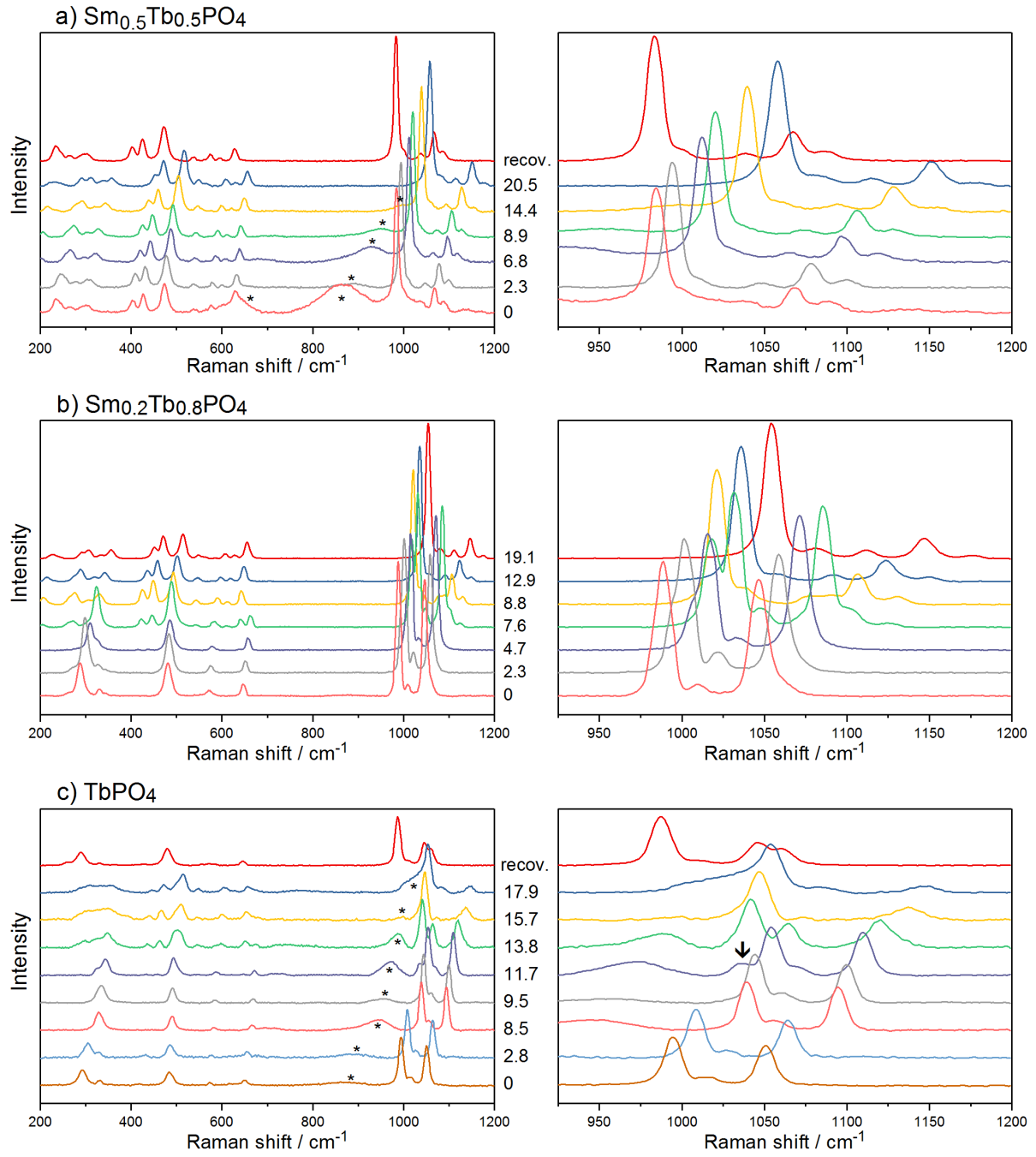


Fig. 10 Pressure dependence of selected Raman spectra of a) $\text{Sm}_{0.5}\text{Tb}_{0.5}\text{PO}_4$ (monazite), b) $\text{Sm}_{0.2}\text{Tb}_{0.8}\text{PO}_4$ (xenotime-structured phase) and c) TbPO_4 (xenotime). Left: Whole recorded range; right: region of stretching vibrations ν_1 and ν_3 . The arrow depicted in c) (right) indicates the appearance of the monazite-type phase (* = broad fluorescence line resulting from the ruby). The pressure values are given in GPa.

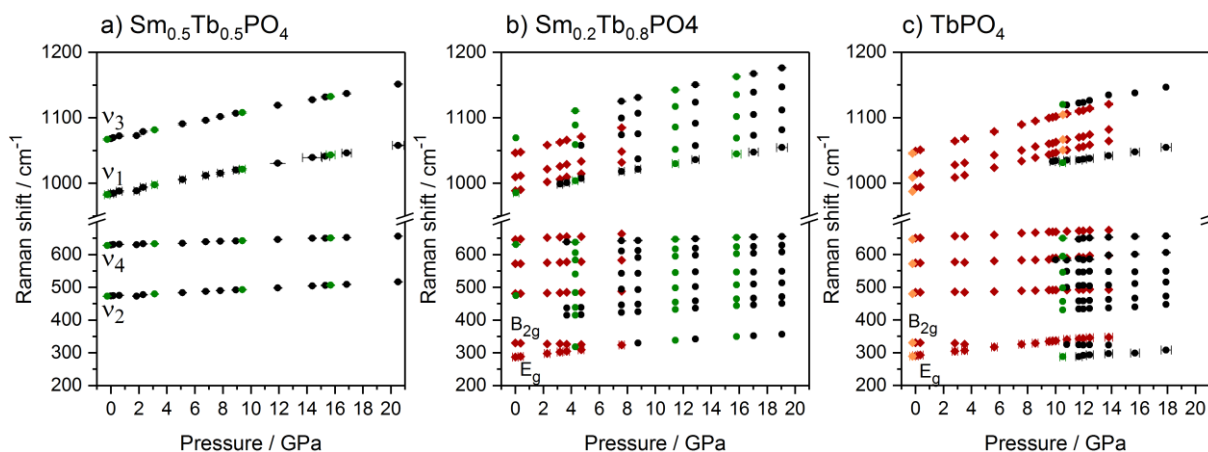


Fig. 11 Evolution of selected Raman band positions of a) $\text{Sm}_{0.5}\text{Tb}_{0.5}\text{PO}_4$ (monazite main bands of normal modes), b) $\text{Sm}_{0.2}\text{Tb}_{0.8}\text{PO}_4$ (pos. 1, xenotime-type phase at ambient pressure), and c) TbPO_4 (xenotime) with increasing (black circle = monazite, red diamond = xenotime) and decreasing pressure (green circle = monazite, yellow diamond = xenotime). The error bars are similar to the size of the symbols.

For the $\text{Sm}_{0.2}\text{Tb}_{0.8}\text{PO}_4$ sample comprising the two co-existing monazite- and xenotime-type phases at ambient pressure, it was possible to obtain spectra from single-phase $\text{Sm}_{0.2}\text{Tb}_{0.8}\text{PO}_4$ -xenotime in the diamond anvil cell (pos. 1, fig. 10b). Spectra recorded at a different sample location were indicative for a phase mixture (pos. 2, spectra shown in figure S2 the supporting information).

On compression, initially all but one Raman bands are shifting to higher wavenumbers. The exception is the B_{2g} mode, which corresponds to a symmetric bending vibration ν_2 , that shifts to lower wavenumbers and increasingly overlaps with the adjacent (rotational) E_g mode. A further pressure increase above 3.2 GPa induces more substantial changes in the Raman spectra. Additional Raman bands appear that can be attributed to the transformation into the monazite high-pressure polymorph. The onset of the phase transformation is shown by the emergence of a ν_1 -vibration at about 1000 cm^{-1} , which becomes more intense with increasing pressure (cf. fig. 11b). The Raman spectra indicate that at pressures of $\geq 8\text{ GPa}$ the phase transformation into the monazite structure is complete. As expected, $\text{Sm}_{0.2}\text{Tb}_{0.8}\text{PO}_4$ -monazite remains stable on further pressure increase up to the maximum pressure achieved in the experiment ($\sim 19\text{ GPa}$). During and after the release of pressure the monazite phase does not transform back into the xenotime-type polymorph (cf. fig. 10 and 11b), which is not consistent with the results of the high-pressure XRD measurements. The same behaviour was also observed in the spectra obtained from the phase mixture (pos. 2, see fig. S2 in the supporting material), where the bands associated with the xenotime-type structure vanish at about 7.5 GPa due to the phase transformation, while the monazite bands are still present up to 19 GPa, and where after pressure release, only the bands of a monazite phase can be observed.

Selected high-pressure Raman spectra of the endmember TbPO_4 are depicted in figure 10c. The pressure-induced changes in band positions on increasing and decreasing pressures are plotted in figure 11c.

The spectrum at ambient conditions is characteristic for xenotime-type compounds [76,83]. Similar trends as for $\text{Sm}_{1-x}\text{Tb}_x\text{PO}_4$ xenotime are observed for TbPO_4 regarding the initial shift of Raman modes on pressure increase. Apart from the B_{2g} mode, all bands shift to higher frequencies with increasing pressure, as already seen for $\text{Sm}_{0.2}\text{Tb}_{0.8}\text{PO}_4$ xenotime. At a pressure of 9.8 GPa monazite is formed and the increase of wavenumbers of the associated Raman modes proceeds with further pressure increase. The modes characteristic for xenotime-type phases can be observed up to a pressure of about 14 GPa. The high pressure monazite-type phase is stable up to the maximum pressure reached in this experiment (approx. 18 GPa). On

pressure release, the Raman spectra indicate that the high pressure Tb-monazite phase transforms back into the polymorph with xenotime structure in the pressure interval from ~14 to 10 GPa (cf. fig. 10 and 11c).

Discussion of the high-pressure experiments

The high-pressure experiments on monazite phases, investigated on the endmember SmPO_4 and the solid solution $\text{Sm}_{0.5}\text{Tb}_{0.5}\text{PO}_4$, show that the structure of monazite is compressed and decompressed gradually. However, a phase transition does not occur up to 35 to 40 GPa; thus Sm-monazite exhibits a high stability under increasing pressure. This agrees well with other high-pressure studies on monazite endmembers with *Ln* cations larger than La and smaller than Tb, where phase stability was reported for up to 30 GPa [51,52].

The solid solution of $\text{Sm}_{0.2}\text{Tb}_{0.8}\text{PO}_4$ xenotime is transformed into the monazite structure at elevated pressures. The beginning of this phase transformation could be observed in Raman spectra already at lower pressures compared to the high-pressure XRD experiments. The powder sample measured by XRD consisted of a ~50/50 monazite-xenotime-mixture. Therefore, the observation of the gradual decrease of the xenotime phase going along with an increase in monazite phase, respectively, is impeded. However, the complete transformation from xenotime into monazite is detectable in the high-pressure XRD powder patterns. After the pressure release, again both phases are observed in the XRD patterns with an increased amount of the monazite phase. Therefore, the high-pressure monazite phase partly retransformed to xenotime after pressure release and partly remained in the monazite structure, due to a quenching of the sample. In contrast to that, the Raman spectrum after pressure release revealed only the monazite phase. However, small amounts of xenotime possibly stayed undetected due to the poor quality of the Raman spectrum of the recovered sample.

For the endmember TbPO_4 xenotime pressure-induced phase transition into monazite was observed. First evidence of a high-pressure monazite phase is given at 9.8 GPa with both techniques. XRD patterns as well as Raman spectra reveal the retransformation into the xenotime structure. However, a small amount of the high-pressure monazite phase was still metastably existing after pressure release in the XRD measurements due to a quenching of the sample. In general, the transformation is reversible.

In comparison to the xenotime-type solid solution $\text{Sm}_{0.2}\text{Tb}_{0.8}\text{PO}_4$, the endmember TbPO_4 comprises a lower disorder or distortion, respectively. In general, the different ionic radii of Sm^{3+} and Tb^{3+} cause tensions in the regularly coordinated LnO_8 polyhedra of the xenotime structure. Therefore, the irregular coordinated LnO_9 in the monazite structure is favoured. The Sm content lowers the activation energy for the phase transition from xenotime to monazite which can be seen in the lower pressure required for the phase transformation in $\text{Sm}_{0.2}\text{Tb}_{0.8}\text{PO}_4$ compared to TbPO_4 .

TbPO_4 xenotime has been previously studied under high pressure [43-45] and a phase transformation to the monazite structure was observed in the same pressure range as in the present study. A co-existence of both phases was described up to 10 GPa [43,44] and up to 14 GPa [45], respectively and the onset of the transformation agrees perfectly with the present data. The opposing shift and softening of the B_{2g} mode was also observed [43-45] and ascribed to the beginning of the phase transition. However, the observed behaviour of the Tb-endmember under pressure release is significantly different to previous experiments. While the phase transformation of Tb-xenotime to Tb-monazite has been thought to be irreversible so far [43,44] or the observations are inconsistent [45], this study clearly demonstrates the reversibility of the pressure-induced transformation of xenotime into monazite.

This is even more remarkable as the number of data points obtained during decompression of TbPO_4 within this work indicates a significant faster pressure release compared to the experiments of Tatsi et al. [44]. Hence,

a quenching of the high pressure monazite phase would have been more likely in the present study and it partly occurred. Hay et al. [48] also observed a back transformation from monazite to xenotime in TEM investigations of a TbPO_4 sample that had been transformed from xenotime to monazite by nano-indentation several months before. While Lacomba-Perales et al. [52] observed a reversible pressure-induced xenotime-monazite transition for ErPO_4 and YPO_4 , Errandonea et al. [84] and Yuan et al. [85] found an irreversible transformation for PrVO_4 and CeVO_4 which also crystallize in the zircon structure. Lacomba-Perales et al. [52] suggested the observed reversibility of the transformation might be related to the effect of the used pressure transmitting medium and the hydrostatic conditions. However, the pressure transmitting media in the present study and in the study of [45] was the same and can thus not explain the different results.

Conclusions

The solid solution series of $\text{Sm}_{1-x}\text{Tb}_x\text{PO}_4$ ($x = 0-1$) was synthesized and characterized in this study. The monazite structure is the dominating phase up to $x = 0.75$. At $x = 0.8$ xenotime and monazite both occur as main phases at about equal amounts. The endmember TbPO_4 clearly exhibits xenotime as the main phase. Additionally, a phase with anhydrite structure could be ascertained in compositions with $x \geq 0.8$ as a consequence of a phase transition from xenotime induced by mechanical stress at low pressures. The detailed phase analyses of the monazite solid solutions ($x \leq 0.8$) confirmed the formation of regular solid solutions and imply that no preferential incorporation of dopants on host cation sites with similarly sized cationic radii occurs. EXAFS analysis reveals an increasing distortion in the solid solution due to different Ln-O bond lengths.

Moreover, the behaviour under pressure of four selected compositions showing monazite ($x = 0$ and 0.5), xenotime ($x = 1.0$) or a mixture of both phases ($x = 0.8$) was investigated by *in situ* high-pressure XRD as well as Raman experiments up to ~ 40 GPa. High-pressure experiments of the monazite phases SmPO_4 and the solid solutions $\text{Sm}_{0.5}\text{Tb}_{0.5}\text{PO}_4$ and $\text{Sm}_{0.2}\text{Tb}_{0.8}\text{PO}_4$ show a steady compression of the crystal lattice with increasing pressure. Therefore, the monazite crystal structure remains stable at elevated pressures. In contrast, xenotime phases with compositions of $\text{Sm}_{0.2}\text{Tb}_{0.8}\text{PO}_4$ and TbPO_4 reveal a phase transition into the monazite structure at about 3.2 and 9.8 GPa, respectively. This study demonstrates for $(\text{Sm,Tb})\text{PO}_4$, that the pressure-induced xenotime-monazite phase transformation is reversible.

These results contribute to examinations on structural changes in Ln -orthophosphates that cannot only occur at high pressures, but can also be induced by local tensions and stress within the crystal structure.

Acknowledgements

The authors would like to thank M. Klinkenberg and M. Güngör for SEM pictures and EDS measurements. Further, we gratefully acknowledge the financial support of the German Federal Ministry of Education and Research (BMBF) within the joint research project "Conditioning" (02NUK021A, 02NUK021F). J. M. Heuser and H. Schlenz thank the Deutsche Forschungsgemeinschaft (DFG) for funding under grant SCHL 495/3-1. Financial support from the BMBF project "ImmoRad" (02NUK019E) is acknowledged by J. D. Bauer.

A part of this work was performed at HPCAT (Sector 16), Advanced Photon Source (APS), Argonne National Laboratory. HPCAT operations are supported by DOE-NNSA under Award No. DE-NA0001974 and DOE-BES under Award No. DE-FG02-99ER45775, with partial instrumentation funding by NSF. This research used resources at the Advanced Photon Source, a U.S. Department of Energy (DOE) Office of Science User Facility operated for the DOE Office of Science by Argonne National Laboratory under Contract No. DE-AC02-

06CH11357. HPCAT beamtime was granted by the Carnegie/DOE Alliance Center (CDAC). M. Lang and J. Cooper acknowledge support by the Office of Basic Energy Sciences of the U.S. Department of Energy as part of the Materials Science of Actinides Energy Frontier Research Center (DE-SC0001089). R. I. Palomares gratefully acknowledges support from the U.S. Department of Energy (DOE) National Nuclear Security Administration (NNSA) through the Carnegie DOE Alliance Center (CDAC) under grant number DE-NA-0002006.

References

- [1] J.-M. Montel, S. Foret, M. Veschambre, C. Nicollet, A. Provost, Electron microprobe dating of monazite, *Chemical Geology* 131 (1-4) (1996) 37-53.
- [2] A. M. Seydoux-Guillaume, R. Wirth, L. Nasdala, M. Gottschalk, J. M. Montel, W. Heinrich, An XRD, TEM and Raman study of experimentally annealed natural monazite, *Physics and Chemistry of Minerals* 29 (2002) 240-253.
- [3] B. Rasmussen, I. R. Fletcher, J. R. Muhling, *In situ* U-Pb dating and element mapping of three generations of monazite: Unravelling cryptic tectonothermal events in low-grade terranes, *Geochimica et Cosmochimica Acta* 71 (3) (2007) 670-690.
- [4] K. Suzuki, T. Kato, CHIME dating of monazite, xenotime, zircon and polycrase: Protocol, pitfalls and chemical criterion of possibly discordant age data, *Gondwana Research* 14 (4) (2008) 569-586.
- [5] A.-M. Seydoux-Guillaume, J.-M. Montel, B. Bingen, V. Bosse, P. de Parseval, J.-L. Paquette, E. Janots, R. Wirth, Low-temperature alteration of monazite: Fluid mediated coupled dissolution-precipitation, irradiation damage, and disturbance of the U-Pb and Th-Pb chronometers, *Chemical Geology* 330/331 (2012) 140-158.
- [6] D. R. Reddy, V. S. S. Prasad, Thorium-rich monazites from the beach sands of Kalingapatnam - Baruva Coast, Andhra Pradesh, East Coast of India, *Current Science* 73 (10) (1997) 880-882.
- [7] N. Clavier, R. Podor, N. Dacheux, Crystal chemistry of the monazite structure, *Journal of the European Ceramic Society* 31 (6) (2011) 941-976.
- [8] N. Dacheux, N. Clavier, R. Podor, Versatile monazite: Resolving geological records and solving challenges in materials science - Monazite as a promising long-term radioactive waste matrix: Benefits of high-structural flexibility and chemical durability, *American Mineralogist* 98 (5-6) (2013) 833-847.
- [9] P. E. D. Morgan, D. B. Marshall, Ceramic Composites of Monazite and 360 Alumina, *Journal of the American Ceramic Society* 78 (6) (1995) 1553-1563.
- [10] D. B. Marshall, P. E. D. Morgan, R. M. Housley, J. T. Cheung, High temperature stability of the Al_2O_3 - LaPO_4 system, *Journal of the American Ceramic Society* 81 (4) (1998) 951-956.
- [11] J. Davis, D. Marshall, K. Oka, R. Housley, P. Morgan, Ceramic composites for thermal protection systems, *Composites Part A: Applied Science and Manufacturing* 30 (4) (1999) 483-488.
- [12] W. Min, D. Miyahara, K. Yokoi, T. Yamaguchi, K. Daimon, Y. Hikichi, T. Matsubara, T. Ota, Thermal and mechanical properties of sintered LaPO_4 - Al_2O_3 composites, *Materials Research Bulletin* 36 (2001) 939-945.
- [13] O. Sudre, J. Cheung, D. Marshall, P. Morgan, C. G. Levi, Thermal insulation coatings of LaPO_4 , in: 25th Annual Conference on Composites, Advanced Ceramics, Materials, and Structures: B (2001) 367-374.
- [14] T. Sekino, T. Kusunose, A. T. Hirvonen, S. H. Kim, Thermal properties and microstructure of zirconia/monazite-type LaPO_4 composites for powder preparation methods, in: *Eco-Materials Processing and Design VIII*, 544 (2007) 909-912.
- [15] R. Yu, L. C. De Jonghe, Proton-Transfer Mechanism in LaPO_4 , *Journal of Physical Chemistry C* 111 (29) (2007) 11003-11007.
- [16] T. Anfimova, Q. F. Li, J. O. Jensen, N. J. Bjerrum, Thermal stability and proton conductivity of rare earth orthophosphate hydrates, *International Journal of Electrochemical Science* 9 (5) (2014) 2285-2300.

- [17] Y. Takita, K. Sano, T. Muraya, H. Nishiguchi, N. Kawata, M. Ito, T. Akbay, T. Ishihara, Oxidative dehydrogenation of iso-butane to isobutene II. Rare earth phosphate catalysts, *Applied Catalysis A: General* 170 (1) (1998) 23-31.
- [18] G. Chen, J. Hölsä, J. Peterson, A luminescence study of single-crystal EuPO_4 at high pressure, *Journal of Physics and Chemistry of Solids* 58 (12) (1997) 2031-2037.
- [19] M. Yu, J. Lin, Y. H. Zhou, M. L. Pang, X. M. Han, S. B. Wang, Luminescence properties of $\text{RP}_{1-x}\text{V}_x\text{O}_4\text{:A}$ ($\text{R}=\text{Y, Gd, La}$; $\text{A}=\text{Sm}^{3+}, \text{Er}^{3+}$ $x=0, 0.5, 1$) thin films prepared by Pechini sol-gel process, *Thin Solid Films* 444 (1-2) (2003) 245-253.
- [20] Z.-G. Yan, Y.-W. Zhang, L.-P. You, R. Si, C.-H. Yan, Controlled synthesis and characterization of monazite type monocrystalline nanowires of mixed lanthanide orthophosphates, *Solid State Communications* 130 (12) (2004) 125-129.
- [21] L. A. Boatner, B. C. Sales, Monazite, in: W. Lutze, R. C. Ewing (Eds.), *Radioactive Waste Forms for the Future*, North-Holland Physics Publishing, Amsterdam (1988) 495-564.
- [22] R. C. Ewing, L. Wang, Phosphates as nuclear waste forms, *Reviews in Mineralogy and Geochemistry* 48 (1) (2002) 673-699.
- [23] N. Dacheux, N. Clavier, A.-C. Robisson, O. Terra, F. Audubert, J. Éric Lartigue, C. Guy, Immobilisation of actinides in phosphate matrices, *Comptes Rendus Chimie* 7 (12) (2004) 1141-1152.
- [24] G. R. Lumpkin, Ceramic waste forms for actinides, *Elements* 2 (6) (2006) 365-372.
- [25] E. H. Oelkers, J.-M. Montel, Phosphates and nuclear waste storage, *Elements* 4 (2008) 113-116.
- [26] W. J. Weber, A. Navrotsky, S. Stefanovsky, E. R. Vance, E. Vernaz, Materials science of high-level nuclear waste immobilization, *MRS Bulletin* 34 (1) (2009) 46-53.
- [27] G. Deissmann, S. Neumeier, G. Modolo, D. Bosbach, Durability of potential plutonium wasteforms under repository conditions, *Mineralogical Magazine* 76 (8) (2012) 2911-2918.
- [28] H. Schlenz, J. Heuser, A. Neumann, S. Schmitz, D. Bosbach, Monazite as a suitable actinide waste form, *Zeitschrift für Kristallographie* 228 (2013) 113-123.
- [29] S. Neumeier, Y. Arinicheva, Y. Ji, J. M. Heuser, P. M. Kowalski, P. Kegler, H. Schlenz, D. Bosbach, G. Deissmann, New insights into phosphate based materials for the immobilisation of actinides, *Radiochim. Acta* (2017).
- [30] Y. Ni, J. M. Hughes, A. N. Mariano, Crystal chemistry of the monazite and xenotime structures, *American Mineralogist* 80 (1995) 21-26.
- [31] S. Ushakov, K. Helean, A. Navrotsky, L. Boatner, Thermochemistry of rare-earth orthophosphates, *Journal of Materials Research* 16 (2001) 2623-2633.
- [32] J. M. Heuser, *Keramiken des Monazit-Typs zur Immobilisierung von minoren Actinoiden und Plutonium*, PhD thesis, RWTH Aachen University; Schriften des Forschungszentrums Jülich Reihe Energie & Umwelt / Energy & Environment 278 (2015).
- [33] Y. Hikichi, K. ito Hukuo, J. Shiokawa, Syntheses of rare earth orthophosphates, *Bulletin of the Chemical Society of Japan* 51 (12) (1978) 3645-3646.

- [34] L. A. Boatner, Synthesis, structure, and properties of monazite, pretulite, and xenotime, *Reviews in Mineralogy and Geochemistry* 48 (2002) 87-121.
- [35] P. Mogilevsky, On the miscibility gap in monazite-xenotime systems, *Physics and Chemistry of Minerals* 34 (2007) 201-214.
- [36] F. Brandt, S. Neumeier, T. Schuppik, Y. Arinicheva, A. Bukaemskiy, G. Modolo, D. Bosbach, Conditioning of minor actinides in lanthanum monazite ceramics: A surrogate study with europium, *Progress in Nuclear Energy* 72 (2014) 140-143.
- [37] P. M. Kowalski, G. Beridze, V. L. Vinograd, D. Bosbach, Heat capacities of lanthanide and actinide monazite-type ceramics, *Journal of Nuclear Materials* 464 (2015) 147-154.
- [38] S. Neumeier, Y. Arinicheva, N. Clavier, R. Podor, A. Bukaemskiy, G. Modolo, N. Dacheux, D. Bosbach, The effect of the synthesis route of monazite precursors on the microstructure of sintered pellets, *Progress in Nuclear Energy* 92 (2016) 298-305.
- [39] A. Hirsch, P. Kegler, I. Alencar, J. Ruiz-Fuertes, A. Shelyug, L. Peters, C. Schreinemachers, A. Neumann, S. Neumeier, H.-P. Liermann, A. Navrotsky, G. Roth, Structural, vibrational, and thermochemical properties of the monazite-type solid solution $\text{La}_{1-x}\text{Pr}_x\text{PO}_4$, *Journal of Solid State Chemistry* 245 (2017) 82-88.
- [40] R. D. Shannon, Revised effective ionic radii and systematic studies of interatomic distances in halides and chalcogenides, *Acta Crystallographica A* 32 (1976) 751-767.
- [41] J. P. Bastide, Systématique simplifiée des composés ABX_4 ($X = \text{O}^{2-}, \text{F}^-$) et évolution possible de leurs structures cristallines sous pression, *Journal of Solid State Chemistry* 71 (1) (1987) 115-120.
- [42] R. Hay, P. Mogilevsky, E. Boakye, Phase transformations in xenotime rare-earth orthophosphates, *Acta Materialia* 61 (18) (2013) 6933-6947.
- [43] E. Stavrou, A. Tatsi, E. Salpea, Y. C. Boulmetis, A. G. Kontos, Y. S. Raptis, C. Raptis, Raman study of zircon-structured RPO_4 ($R = \text{Y}, \text{Tb}, \text{Er}, \text{Tm}$) phosphates at high pressures, *Journal of Physics: Conference Series* 121 (4) (2008) 042016-(1-6).
- [44] A. Tatsi, E. Stavrou, Y. C. Boulmetis, A. G. Kontos, Y. S. Raptis, C. Raptis, Raman study of tetragonal TbPO_4 and observation of a first-order phase transition at high pressure, *Journal of Physics: Condensed Matter* 20 (42) (2008) 425216-(1-7).
- [45] J. López-Solano, P. Rodríguez-Hernández, A. Muñoz, O. Gomis, D. Santamaría-Pérez, D. Errandonea, F. J. Manjón, R. S. Kumar, E. Stavrou, C. Raptis, Theoretical and experimental study of the structural stability of TbPO_4 at high pressures, *Physical Review B* 81 (14) (2010) 144126-(1-9).
- [46] R. S. Hay, E. E. Boakye, P. Mogilevsky, G. E. Fair, T. A. Parthasarathy, J. E. Davis, Transformation plasticity in $(\text{Gd}_x\text{Dy}_{1-x})\text{PO}_4$ fiber coatings during fiber push out, *Journal of the American Ceramic Society* 96 (5) (2013) 1586-1595.
- [47] R. S. Hay, E. E. Boakye, P. Mogilevsky, Transformation plasticity in TbPO_4 and $(\text{Gd,Dy})\text{PO}_4$ orthophosphates during indentation of polycrystalline specimens, *Journal of the European Ceramic Society* 34 (3) (2014) 773-781.
- [48] R. S. Hay, G. E. Fair, E. E. Boakye, P. Mogilevsky, T. A. Parthasarathy, J. Davis, Softening of rare earth orthophosphates by transformation plasticity: possible applications to fiber-matrix interphases in ceramic

composites, in: D. Singh, D. Zhu, Y. Zhou, M. Singh (Eds.), *Design, Development, and Applications of Engineering Ceramics and Composites: Ceramic Transactions*, John Wiley & Sons, 2010.

[49] R. S. Hay, G. E. Fair, E. E. Boakye, P. Mogilevsky, T. A. Parthasarathy, M. Ahrens, T. J. Godar, Transmission electron microscopy of rare-earth orthophosphate fibre-matrix interphases that deform by transformation plasticity during fiber push-out, in: *Mechanical Properties and Performance of Engineering Ceramics and Composites VI: Ceramic Engineering and Science Proceedings*, John Wiley & Sons, 2011.

[50] J. W. Christian, G. B. Olson, M. Cohen, Classification of displacive transformation (what is martensite?), Colloque C8, supplement au Journal de Physique III 5 (1995) C8-3-C8-10.

[51] T. Huang, J.-S. Lee, J. Kung, C.-M. Lin, Study of monazite under high pressure, *Solid State Communications* 150 (37-38) (2010) 1845-1850.

[52] R. Lacomba-Perales, D. Errandonea, Y. Meng, M. Bettinelli, High-pressure stability and compressibility of APO_4 ($A = \text{La, Nd, Eu, Gd, Er, and Y}$) orthophosphates: An X-ray diffraction study using synchrotron radiation, *Physical Review B* 81 (6) (2010) 064113-(1-9).

[53] D. Errandonea, O. Gomis, P. Rodríguez-Hernández, A. Muñoz, J. Ruiz-Fuertes, M. Gupta, S. N. N Achary, A. Hirsch, F. J. Manjón, L. Peters, G. Roth, A. K. Tyagi, M. Bettinelli, High-pressure structural and vibrational properties of monazite-type BiPO_4 , LaPO_4 , CePO_4 and PrPO_4 , *Journal of Physics: Condensed Matter* (2017, in press).

[54] P. Raison, S. Heathman, G. Wallez, C. Zvoriste, D. Bykov, G. Menard, E. Suard, K. Popa, N. Dacheux, R. Konings, R. Caciuffo, Structure and nuclear density distribution in the cheralite - $\text{CaTh}(\text{PO}_4)_2$: studies of its behaviour under high pressure (36 GPa), *Physics and Chemistry of Minerals* 39 (2012) 685-692.

[55] J. Ruiz-Fuertes, A. Hirsch, A. Friedrich, B. Winkler, L. Bayarjargal, W. Morgenroth, L. Peters, G. Roth, V. Milman, High-pressure phase of LaPO_4 studied by X-ray diffraction and second harmonic generation, *Phys. Rev. B* 94 (2016) 134109.

[56] E. E. Boakye, P. Mogilevsky, R. S. Hay, G. E. Fair, Synthesis and phase composition of lanthanide phosphate nanoparticles LnPO_4 ($\text{Ln} = \text{La, Gd, Tb, Dy, Y}$) and solid solutions for fiber coatings, *Journal of the American Ceramic Society* 91 (12) (2008) 3841-3849.

[57] H. M. Rietveld, Line profiles of neutron powder-diffraction peaks for structure refinement, *Acta Crystallography* 22 (1) (1967) 151-152.

[58] A. Coelho, TOPAS Academic User Manual. Version 4.1. Coelho Software, Brisbane, Australia (2007).

[59] R. W. Cheary, A. Coelho, A fundamental parameters approach to X-ray line-profile fitting. *Journal of Applied Crystallography* 25 (2) (1992) 109-121.

[60] S. M. Antao, Crystal-structure analysis of four mineral samples of anhydrite, CaSO_4 , using synchrotron high-resolution powder X-ray diffraction data. *Powder Diffraction* 26 (4) (2011) 326-330.

[61] S. M. Webb, SIXpack: a graphical user interface for XAS analysis using IFEFFIT, *Physica Scripta*, 2005, T115.

[62] T. Ressler, WinXAS: a program for X-ray absorption spectroscopy data analysis under MSWindows. *Journal of Synchrotron Radiation* 5 (1998) 118-122.

- [63] A. L. Ankudinov, J. J. Rehr, Relativistic calculations of spin-dependent x-ray-absorption spectra, *Phys. Rev. B* 56 (1997) R1712-R1715.
- [64] C. Prescher, V. B. Prakapenka, DIOPTAS: a program for reduction of two-dimensional X-ray diffraction data and data exploration, *High Pressure Research* 35:3 (2015) 223-230.
- [65] B. H. Toby and R. B. Von Dreele, GSAS-II: the genesis of a modern open-source all purpose crystallography software package, *J. Appl. Cryst.* 46 (2013) 544–549.
- [66] R. Boehler, New diamond cell for single-crystal X-ray diffraction, *Review of scientific instruments* 77 (11) (2006) 115103-(1-3).
- [67] H. K. Mao, J. Xu, P. M. Bell, Calibration of the ruby pressure gauge to 800 kbar under quasi-hydrostatic conditions, *Journal of Geophysical Research* 91 (B5) (1986) 4673-4676.
- [68] P. A. Temple, C. E. Hathaway, Multiphonon Raman Spectrum of Silicon, *Phys. Rev. B* 7 (1973) 3685-3697.
- [69] A. Hezel, S. D. Ross, Forbidden transitions in the infra-red spectra of tetrahedral anions—III. Spectra-structure correlations in perchlorates, sulphates and phosphates of the formula MXO_4 , *Spectrochimica Acta* 22 (1966) 1949-1961.
- [70] M. Ferhi, K. Horchani-Naifer, M. Férid, Hydrothermal synthesis and photoluminescence of the monophosphate $LaPO_4:Eu(5\%)$. *Journal of Luminescence* 128(11) (2008) 1777-1782.
- [71] L. Chunhua, H. Jie, X. Zhongzi, and N. Yaru. Preparation and IR spectra study of rare earth orthophosphates. *Journal of Rare Earths* 25 (2007) 273–276.
- [72] J. Heuser, Raman and infrared spectroscopy of monazite-type ceramics used for nuclear waste conditioning, *Progress in Nuclear Energy* 72 (2014) 149-155.
- [73] O. Terra, N. Clavier, N. Dacheux, R. Podor, Preparation and characterization of lanthanum-gadolinium monazites as ceramics for radioactive waste storage, *New Journal of Chemistry* 27 (6) (2003) 957–967.
- [74] K. Ruschel, L. Nasdala, A. Kronz, J. M. Hanchar, D. M. Tobbens, R. Skoda, F. Finger, A. Moller, A Raman spectroscopic study on the structural disorder of monazite-(Ce), *Mineralogie and Petrology* 105 (1–2) (2012) 41–55.
- [75] S. Neumeier, P. Kegler, Y. Arinicheva, A. Shelyug, P. M. Kowalski, C. Schreinemachers, A. Navrotsky, D. Bosbach, Thermochemistry of $La_{1-x}Ln_xPO_4$ -monazites ($Ln = Gd, Eu$), *The Journal of Chemical Thermodynamics*, 105 (2017) 396–403.
- [76] G. M. Begun, G. W. Beall, L. A. Boatner, W. J. Gregor, Raman spectra of the rare earth orthophosphates, *Journal of Raman Spectroscopy* 11 (4) (1981) 273-278.
- [77] D. E. Hobart, G. M. Begun, R. G. Haire, H. E. Hellwege, Raman-spectra of the transplutonium orthophosphates and trimetaphosphates, *J. Raman Spectrosc.* 14 (1) (1983) 59–62.
- [78] R. Podor, Raman spectra of the actinide-bearing monazites, *European Journal of Mineralogy* 7 (6) (1995) 1353–1360.
- [79] C. Santos, E. Silva, A. Ayala, I. Guedes, P. Pizani, C.-K. Loong, L. A. Boatner, Raman investigations of rare earth orthovanadates, *Journal of Applied Physics* 101 (5) (2007) 053511.

- [80] A. Rossberg, T. Reich, G. Bernhard, Complexation of uranium(VI) with protocatechuic acid - application of iterative transformation factor analysis to EXAFS spectroscopy. *Analytical and Bioanalytical Chemistry* 376 (5) (2003) 631-638.
- [81] A. Rossberg, K.-U. Ulrich, S. Weiss, S. Tsushima, T. Hiemstra, A. C. Scheinost, Identification of uranyl surface complexes on ferrihydrite: Advanced EXAFS data analysis and CD-MUSIC modeling, *Environ. Sci. Technol.* 43 (2009) 1400–1406.
- [82] O. Tschauner, S. V. Ushakov, A. Navrotsky, L. A. Boatner, Phase transformations and indications for acoustic mode softening in Tb-Gd orthophosphate, *Journal of Physics: Condensed Matter* 28 (3) (2016) 035403.
- [83] P. Dawson, M. M. Hargreave, G. R. Wilkinson, The vibrational spectrum of zircon (ZrSiO_4), *Journal of Physics C: Solid State Physics* 4 (2) (1971) 240-256.
- [84] D. Errandonea, S. N. Achary, J. Pellicer-Porres, A. K. Tyagi, Pressure induced transformations in PrVO_4 and SmVO_4 and isolation of high pressure metastable phases, *Inorganic Chemistry* 52 (9) (2013) 5464-5469.
- [85] H. Yuan, K. Wang, C. Wang, B. Zhou, K. Yang, J. Liu, B. Zou, Pressure induced phase transformations of zircon-type LaVO_4 nanorods, *The Journal of Physical Chemistry C* 119 (15) (2015) 8364-8372.

Supporting information

Table S1: Crystal structure information obtained from Rietveld refinements for Sm_{1-x}Tb_xPO₄ monazite (M)-type phases.

<i>x</i>		0	0.2	0.35	0.5	0.65	0.7	0.75	0.8
<i>r</i> / Å		1.132	1.125	1.119	1.114	1.108	1.106	1.104	1.102
Phase		M	M	M	M	M	M	M	M
<i>a</i> / Å		6.69035(4)	6.67673(4)	6.66670(4)	6.65707(6)	6.64616(3)	6.64290(3)	6.63933(3)	6.63707(14)
<i>b</i> / Å		6.89207(4)	6.87610(4)	6.86391(4)	6.85316(6)	6.83970(4)	6.83609(3)	6.83185(3)	6.82891(14)
<i>c</i> / Å		6.37219(4)	6.36197(4)	6.35453(3)	6.34756(5)	6.33876(3)	6.33558(3)	6.33268(3)	6.33282(13)
<i>θ</i> / °		103.8632(4)	103.9084(4)	103.9455(4)	103.9784(6)	104.0210(4)	104.0310(3)	104.0431(3)	104.0595(17)
<i>V</i> / Å ³		285.2647(3)	283.5141(3)	282.2102(3)	281.0123(41)	279.5609(3)	279.1241(2)	278.6586(2)	278.4302(101)
<i>ρ</i> / g/cm ³		5.71237(6)	5.78777(6)	5.84474(5)	5.90001(9)	5.96116(5)	5.98068(4)	6.00087(4)	6.01601(22)
wt%		100	100	100	100	99.374(105)	98.762(89)	98.747(87)	45.737(297)
Ln	<i>x</i>	0.28175(15)	0.28143(16)	0.28144(14)	0.28165(17)	0.28146(13)	0.28149(11)	0.28161(11)	0.28144(58)
	<i>y</i>	0.15682(16)	0.15669(18)	0.15628(15)	0.15516(19)	0.15474(14)	0.15485(12)	0.15466(12)	0.15738(58)
	<i>z</i>	0.09823(17)	0.09764(18)	0.09768(16)	0.09696(20)	0.09695(16)	0.0968(13)	0.09682(13)	0.09795(68)
	<i>B</i> / Å ²	0.28	0.28	0.28	0.28	0.28	0.28	0.28	0.28
P	<i>x</i>	0.30303(49)	0.30335(52)	0.30589(45)	0.30565(53)	0.30604(42)	0.30368(35)	0.30314(36)	0.30368(145)
	<i>y</i>	0.16041(50)	0.16051(53)	0.16238(45)	0.16127(56)	0.16254(43)	0.16347(37)	0.16150(36)	0.14876(166)
	<i>z</i>	0.61252(48)	0.61036(51)	0.60961(44)	0.61158(54)	0.61068(43)	0.61318(35)	0.61117(35)	0.61553(156)
	<i>B</i> / Å ²	0.32	0.32	0.32	0.32	0.32	0.32	0.32	0.32
O1	<i>x</i>	0.24939(129)	0.24298(142)	0.24611(119)	0.24892(145)	0.24823(112)	0.24987(90)	0.24815(90)	0.23291(454)
	<i>y</i>	0.00196(85)	0.00068(89)	-0.00125(75)	0.00092(94)	-0.00220(72)	0.00082(61)	0.00024(60)	-0.00227(236)
	<i>z</i>	0.43236(104)	0.43228(111)	0.43371(97)	0.43308(117)	0.43843(92)	0.43690(76)	0.43261(75)	0.43739(275)
O2	<i>x</i>	0.38771(89)	0.37999(95)	0.38054(83)	0.38742(101)	0.38290(80)	0.38327(59)	0.38418(65)	0.37535(258)
	<i>y</i>	0.33419(87)	0.33572(91)	0.34037(78)	0.33695(98)	0.34034(76)	0.33731(59)	0.33874(63)	0.31366(235)
	<i>z</i>	0.50165(109)	0.49757(115)	0.49782(99)	0.50045(121)	0.50050(94)	0.49996(68)	0.50091(76)	0.48384(267)
O3	<i>x</i>	0.47752(97)	0.48026(101)	0.47645(91)	0.48054(109)	0.47880(85)	0.47730(62)	0.47361(62)	0.49353(252)
	<i>y</i>	0.10836(108)	0.10933(115)	0.10147(97)	0.10834(123)	0.10829(97)	0.11063(73)	0.10109(70)	0.09840(337)
	<i>z</i>	0.81477(91)	0.81124(96)	0.81389(83)	0.81345(102)	0.81405(79)	0.81523(60)	0.81378(59)	0.79654(279)
O4	<i>x</i>	0.12048(71)	0.12033(77)	0.12162(67)	0.12090(83)	0.12070(64)	0.12066(55)	0.12149(54)	0.11182(204)
	<i>y</i>	0.20997(120)	0.20684(128)	0.20911(110)	0.20943(134)	0.20958(104)	0.21285(83)	0.20939(84)	0.18537(434)
	<i>z</i>	0.71353(100)	0.71427(104)	0.71041(91)	0.71358(111)	0.71196(87)	0.71784(73)	0.71754(71)	0.70787(277)
Oi	<i>B</i> / Å ²	0.62	0.62	0.62	0.62	0.62	0.62	0.62	0.62
R_{exp}		1.136	1.100	1.074	1.035	0.982	0.892	0.869	0.983
R_{wp}		2.147	2.232	2.001	2.310	1.872	1.649	1.683	3.535
GoF		1.891	2.028	1.864	2.233	1.906	1.848	1.936	3.596

Table S2: Crystal structure information obtained from Rietveld refinements for Sm_{1-x}Tb_xPO₄ xenotime (X)- and anhydrite (A)-type phases.

<i>x</i>	0.65	0.7	0.75	0.8	1.0	0.8	1.0
<i>r</i> / Å	1.054	1.052	1.050	1.048	1.040	1.048	1.040
Phase	X	X	X	X	X	A	A
<i>a</i> / Å	6.9653(14)	6.9622(6)	6.9581(5)	6.95972(10)	6.94271(7)	6.9555(9)	6.9462(5)
<i>b</i> / Å						6.9580(10)	6.9393(6)
<i>c</i> / Å	6.1351(72)	6.1199(35)	6.1168(32)	6.08976(13)	6.07323(7)	6.1294(6)	6.1423(4)
<i>V</i> / Å ³	297.641(368)	296.641(176)	296.151(163)	294.9746(106)	292.7368(66)	296.6357(63)	296.0669(37)
<i>ρ</i> / g/cm ³	5.5991(70)	5.6275(33)	5.6464(31)	5.67859(20)	5.76085(13)	5.64688(12)	5.6961(7)
wt%	0.626(105)	1.238(89)	1.253(87)	50.268(305)	91.057(302)	3.995(291)	8.943(302)
<i>Ln</i>	<i>x</i>			0	0		
	<i>y</i>			0.75	0.75		
	<i>z</i>			0.125	0.125		
	<i>B</i> / Å ²			0.35	0.35		
<i>P</i>	<i>x</i>			0	0		
	<i>y</i>			0.25	0.25		
	<i>z</i>			0.375	0.375		
	<i>B</i> / Å ²			0.43	0.43		
<i>O1</i>	<i>x</i>			0	0		
	<i>y</i>			0.07650(145)	0.07555(62)		
	<i>z</i>			0.22056(180)	0.21163(82)		
	<i>B</i> / Å ²			0.6	0.6		
<i>R</i> _{exp}	0.982	0.892	0.869	0.983	0.806	0.983	0.806
<i>R</i> _{wp}	1.872	1.649	1.683	3.535	4.485	3.535	4.485
GoF	1.906	1.848	1.936	3.596	5.567	3.596	5.567

Table S3: Summary of pressure induced phase transitions on lanthanide phosphates and LaVO₄.

Composition	Structure “As synth.”	Test method; max. pressure	Characterisation method				Phase after decompression	Ref.
(Gd,Dy)PO ₄ ; TbPO ₄	X	fiber push out; indentation; 10-80 MPa	TEM				X, A, M	[42,46,47]
			Three transformations observed: Low-p: X → A; A → M; assumed to be rev. and high-p: X → M X → A; rev. (high shear stress, low pressure)					
LnPO ₄ , Ln = Y, Er	X	DAC; Ne 28 GPa	XRD		Raman			[52]
			Pressure (GPa)	PT	Pressure (GPa)	PT		
			19.7 – 23.5 (Y)	X → M; rev.				
			17.3 – 23.3 (Er)	X → M; rev.				
LaPO ₄	M	30 GPa	26	M → B; irrev.				
LnPO ₄ Ln = Nd, Eu, Gd	M	28, 25, 30 GPa	30	---				
LaVO ₄ Nanorods	X	DAC; M/E-Mix 12 GPa	5 – 11	X → M; irrev.			M, X	[84]
		DAC; Si-oil 17.2 GPa	12.9	M → undet.; rev.				
LnPO ₄ Ln = Y, Er,	X	DAC; M/E-Mix 7.9				---	X	[43] [#]
Ln = Tb, Tm	X	15.5			9.5 (Tb)	X→M; irrev.	M	

Structure type abbr.: M: monazite; X: xenotime; A: anhydrite; B: barite; PT: Phase transition; [#]These studies were performed on parts of the same TbPO₄ single crystal

DAC: Diamond anvil cell; M/E-Mix: Methanol/Ethanol-Mix

undet.: undetermined

Table S3 Continued: Summary of pressure induced phase transitions on lanthanide phosphates and LaVO₄.

Composition	Structure “As synth.”	Test method; max. pressure	Characterisation method				Phase after decompression	Ref.
			XRD		Raman			
			Pressure (GPa)	PT	Pressure (GPa)	PT		
Gd _{0.5} Tb _{0.5} PO ₄	X	DAC; Ne 10.6 GPa	4.2 – 5.8 10.0 – 10.6	X → A A → M				[81]
TbPO ₄	X	DAC; Ne 16 GPa 25 GPa	9.9 – 13.8 10.2 – 15	X → M; rev. X → M; irrev.			X M, X	[45] [#]
TbPO ₄	X	DAC; M/E-Mix 15.5 GPa			9.5	X→M; irrev.	M	[44] [#]
SmPO ₄	M	DAC; Ne; 41 GPa		---			M	This study
Sm _{0.5} Tb _{0.5} PO ₄	M	DAC; Ne 33 GPa		---			M	
	M	DAC; Ne 21 GPa				---	M	
Sm _{0.2} Tb _{0.8} PO ₄	X, M		grinding	X → A			X, M, A	
Sm _{0.2} Tb _{0.8} PO ₄	X, M	DAC; Ne 20 GPa	9.6 – 13.6	X → M; rev.			X, M	
	X, M	DAC; Ne 19 GPa			3.2 – 8	X→M; irrev.	M	
TbPO ₄	X		grinding	X → A			X, A	
TbPO ₄	X	DAC; Ne 21 GPa	9.8 – 16.8	X → M; rev.			M	
	X	DAC; Ne 18 GPa			9.8 – 14	X→M; rev.	X	

Structure type abbr.: M: monazite; X: xenotime; A: anhydrite; B: barite; PT: Phase transition; [#]These studies were performed on parts of the same TbPO₄ single crystal

DAC: Diamond anvil cell; M/E-Mix: Methanol/Ethanol-Mix

undet.: undetermined

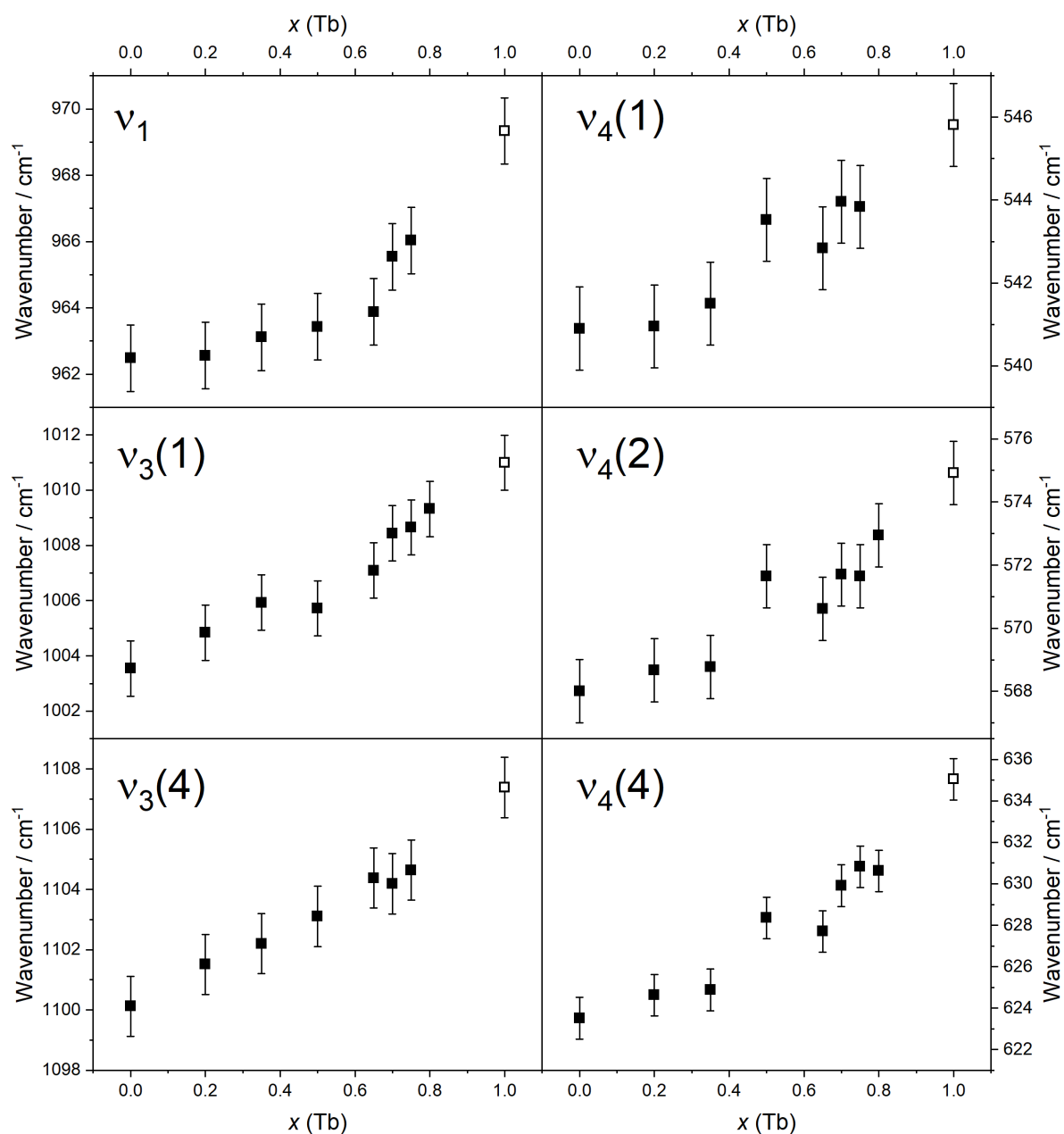


Fig. S1 Selected IR band of Sm_{1-x}Tb_xPO₄ solid solutions with monazite structure. For comparison values for Tb-monazite are plotted with open symbols [32]. To distinguish the vibrations that have split up, increments (i) were added that count up from low to high wavenumbers.

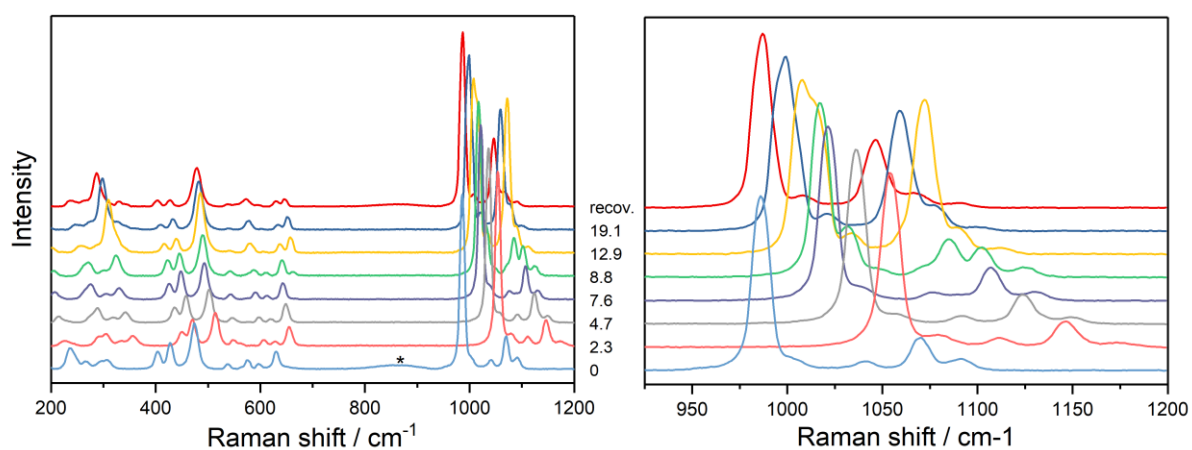


Fig. S2 Pressure dependent Raman spectra of composition $\text{Sm}_{0.2}\text{Tb}_{0.8}\text{PO}_4$ showing both existing phases monazite and xenotime at ambient pressure. The asterisk indicates a broad fluorescence line resulting from the ruby. The pressure values are given in GPa. The spectrum of the recovered sample is shown at the top.